ALMA MATER STUDIORUM
UNIVERSITÀ DI BOLOGNA

DEPARTMENT OF PHYSICS AND ASTRONOMY "A. RIGHI"

SECOND CYCLE DEGREE

PHYSICS

Characterization of muon deep inelastic scattering events in the SND@LHC experiment Monte Carlo simulation

Supervisor
Prof. Luigi Guiducci

Co-supervisors
Giulia Paggi
Filippo Mei

Defended by
Alessia Orlando

Graduation Session March 2026

Academic Year 2024/2025

Abstract

Scattering and Neutrino Detector at the Large Hadron Collider (SND@LHC) is a compact, stand-alone experiment located in the TI18 tunnel (480 m downstream of the ATLAS interaction point) to perform measurements with high-energy neutrinos up to the TeV scale produced at LHC in the pseudorapidity region $7.2 < \eta < 8.4$. The experimental environment is subject to an intense flux of high energy muons, which can interact in the detector material. In particular, muon deep inelastic scattering represents one of the main background sources, as it can mimic the signatures of muon neutrino charged-current interactions. This thesis focuses on the characterization of muon deep inelastic scattering background using Monte Carlo simulations. A comparative study of various simulated samples was performed to evaluate the impact of the evolution of the simulation chain on the modelling of deep inelastic scattering events. Improvements in the the simulation with the latest geometry, including the implementation of a Monte Carlo Event Builder, enabled a preliminary comparison between the simulated events and data for a background evaluation in support of the ongoing muon neutrino charged-current analysis on 2024 data.

Contents

List of Figures

Introduction

Within the Standard Model, neutrinos are among the most elusive and interesting particles. They interact only via weak interaction, making their detection particularly challenging and requiring massive detectors operated in low-background environments. The high energy proton-proton collisions at the Large Hadron Collider (LHC), with a centre of mass energy of 13.6 TeV, provide an intense flux of neutrinos up the TeV energy range.

In this context, the Scattering and Neutrino Detector at LHC (SND@LHC) experiment has been designed to detect neutrinos of all three flavours produced in the forward direction in a pseudorapidity range of $7.2 < \eta < 8.4$, which is not accessible to other LHC experiments. The detector is a hybrid system that combines nuclear emulsions and electronic detectors. The target interleaves tungsten walls with nuclear emulsions and scintillating fibre (SciFi) planes, for a total target mass of about 830 kg, and it serves as a sampling electromagnetic calorimeter. Downstream of the target, a hadronic calorimeter and muon identification system alternates iron slabs and scintillating planes. Upstream of the target, a veto system identifies incoming charged particles.

The detector is located in the TI18 tunnel, 480 m downstream of the ATLAS interaction point. The main background source comes from high-energy muons originating in proton-proton collisions. While the veto system identifies the majority of the muons entering the instrumented volume, a residual background remains. Muons can undergo deep inelastic scattering (DIS) with nucleons in the target, producing hadronic showers that closely mimic muon neutrinos charged-current interactions. To discriminate ν_μ from muons, it is essential to characterize and suppress the muon DIS background; this task relies on Monte Carlo simulations. This work aims to validate the simulation framework and support the ongoing ν_μ analysis on 2024 data.

In Chapter 1, an overview of neutrino physics is provided. It traces the history of the neutrino from hypothesis to discovery and addresses its relevant properties, within and beyond the Standard Model. The chapter reviews the various neutrino interaction cross sections, highlighting the role of the LHC as a neutrino source.

In Chapter 2, the description of the SND@LHC experiment includes its primary physics goals, as well as the design of the subdetectors and the evaluation of the particle flux in the experimental environment.

In Chapter 3, the Monte Carlo simulation framework is presented. This includes the modelling of the particle transport from the proton-proton interaction point to the detector location using FLUKA, followed by the simulations of the physics processes, using GENIE for neutrinos and PYTHIA for muon DIS, and the simulation of the interaction of primary and secondary particles with the detector passive and

active materials using GEANT4. A key focus is placed on the digitization process and the Monte Carlo Event Builder.

In Chapter 4, the characterization of muon DIS events is discussed. This chapter assesses the performance of the simulation chain through the study of some key features of the DIS interaction in various samples, and it concludes with a preliminary comparison with data collected during 2024.

1 Neutrino Physics

1.1 Neutrino hypothesis and discovery

The existence of a neutral, light particle with spin $s = \frac{1}{2}$ was proposed by Pauli in 1930 [1] in order to explain the anomalous energy spectrum of the β decay. In the nuclear β decay an atomic nucleus emits a β particle (electron or positron) transitioning to the neighbouring isobar:

$$(Z, N) \to (Z \pm 1, N \mp 1) + e^{\mp},$$

where Z and N are the number of protons and neutrons in the nucleus, respectively. According to the energy and momentum conservation, the two particles in the final state recoil back-to-back with opposite momentum. The electron, being much smaller than the nucleus, is expected to have a discrete energy spectrum, with a fixed value at the Q-value of the reaction, i.e. the mass difference between (Z, N) and $(Z + 1, N - 1)$. However, experiments showed a continuous spectrum with end-point at the expected value, implying the violation of the energy conservation law. Pauli's hypothesis, in which a third particle was added to the final state to explain the continuous spectrum of the electron, could explain this phenomenon, but the nature of this particle, which he originally called neutron, made it extremely difficult to detect. Two years later, Chadwick discovered the neutron [2], a neutral particle with mass similar to the proton, which therefore could not be Pauli's particle. The latter was then renamed by Fermi as *neutrino* [3].

The neutrino hypothesis initiated the search for this elusive particle, which eventually resulted in its discovery in 1956 at Savannah River. The experiment, led by Cowan and Reines [4], aimed to detect reactor antineutrinos through the inverse β decay on protons:

$$\overline{\nu} + p \to n + e^{+}.$$

After the reaction, the positron annihilates with an electron in the medium within a few nanoseconds emitting two 0.5 MeV γ rays in opposite directions. The two photons are detected through the flashes of visible light produced by a liquid scintillator added to water tanks. In the meantime, the neutron travels in the medium, slowing down as it collides with protons. Enriching the liquid with cadmium salt, the thermalized neutron can be easily captured, exciting the Cd nucleus. In the consequent de-excitation the cadmium emits two 9 MeV γ rays which produce flashes of visible light. This sequence of two flashes of light separated by a few microseconds is the double signature of the inverse β decay, represented in Figure 1.

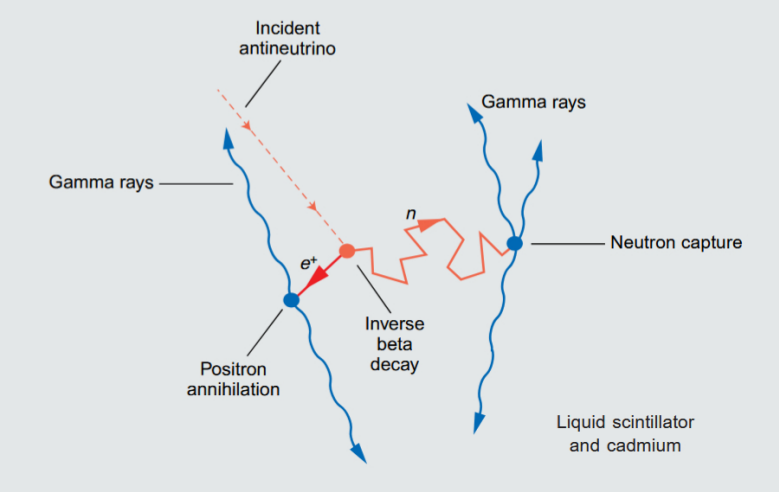

Figure 1: Double signature of the inverse β decay in the Reines and Cowan experiment.

1.2 Neutrino flavours

When the existence of the neutrino was proposed, only two elementary particles were known and the only observed process involving the neutrino was the β decay.

The discovery of the muon in 1937 [5] paved the way to a second type of neutrino, different from the one associated to the electron (ν_e); in particular, the main concern was the nature of the neutrinos involved in the ordinary muon decay $\mu \to e + \nu + \overline{\nu}$. Taking into account also the hypothetical muon decay $\mu \to e + \gamma$, in the hypothesis of only one type of neutrino, the branching ratio $(\mu \to e + \gamma)/(\mu \to e + \nu + \overline{\nu})$ would be of the order of 10^{-4} [6]. However, the branching ratio was measured to be less than 10^{-8} [7], supporting the hypothesis of the existence of a second type of neutrino (ν_μ).

In 1962, Lederman, Schwartz, and Steinberger led an experiment which resulted in the discovery of the ν_μ at the Brookhaven Alternating Gradient Synchrotron (AGS) [8]. The idea behind the experiment was that if $\nu_\mu \neq \nu_e$, between the processes

$$\overline{\nu}_\mu + p \to e^+ + n$$
$$\overline{\nu}_\mu + p \to \mu^+ + n$$

only the latter would be observed [9] and hence an abundance of muons should be detected. The high-energy neutrinos used in the experiment were produced in high-energy pion decays $\pi^\pm \to \mu^\pm + (\nu/\overline{\nu})$ as follows:

- The collision of the proton beam in the AGS onto a target produced charged pions;

- The pions travelled towards a collimator where only π^+ or π^- were selected;
- The pions then entered a vacuum tube where they decayed in $\mu^\pm$ and $\nu/\overline{\nu}$, depending on their charge;
- The emitted charged particle was identified.

The flux of particles hit a 13.5 m-thick iron shield wall at a distance of 21 m from the target; strongly interacting particles were absorbed by nuclear interactions and muons by ionization loss. The neutrino interactions were then observed in 90 aluminium spark chamber planes grouped in ten 1-ton modules. Anticoincidence sheets were added to reduce the effect of cosmic rays and AGS-produced muons penetrating the shield. The layout of the experiment is shown in Figure 2. 113 events were observed; among these, 56 were selected: 34 single muons of more than 300 MeV (Figure 3a) and 22 vertex events originated from more than one track (Figure 3b). Of the 34 single track events, 5 were considered to be cosmic ray background. Supposing $\nu_e = \nu_\mu$, about 29 electron showers were expected, while only 6 were observed. In conclusion, the experimental result was not consistent with the hypothesis of the existence of only one type of neutrino.

Similarly to the case of ν_μ, the discovery of the third charged lepton τ in 1975 [10] led to the postulation of the existence of the tau neutrino ν_τ. The hypothesis was confirmed in 2000 at the DONUT experiment at Fermilab [11], designed to identify the τ produced in neutrino interactions using nuclear emulsions. The neutrino beam was created using 800 GeV protons from the Fermilab Tevatron interacting in a 1 m long tungsten beam dump, 36 m upstream from the emulsion target. Most of the neutrinos interacting in the target were produced in the leptonic decay of D_s to $\tau + \overline{\nu}_\tau$ and the subsequent decay of τ to ν_τ. The detector, represented in Figure 4, consisted of a scintillation counter veto wall, an emulsion-scintillating fibre

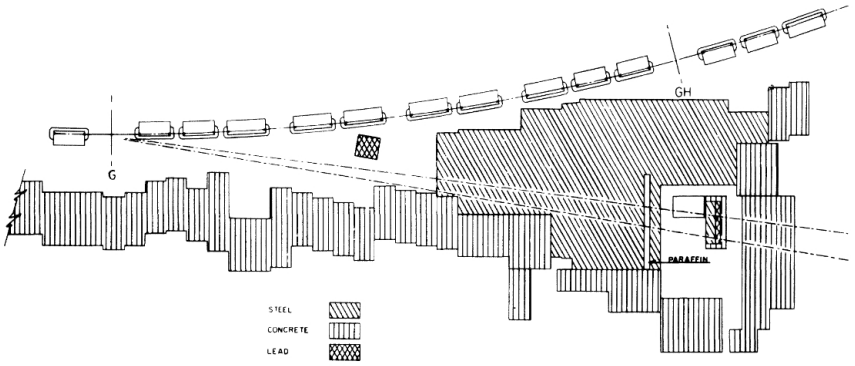

Figure 2: Schematic representation of the AGS neutrino experiment.

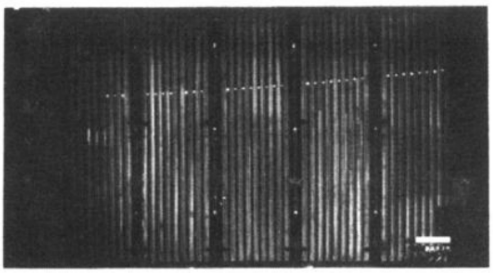

(a) Single muon event with $p_\mu > 700$ MeV.

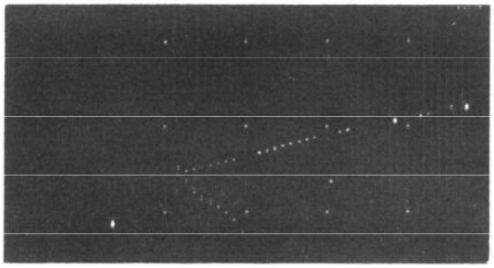

(b) Vertex event with a single muon of $p_\mu > 500$ MeV and an electron-type track.

Figure 3: Selected events in the spark chambers.

hybrid target, trigger hodoscopes, and the charged particle spectrometer. Neutrinos entering the detector interacted with an atomic nucleus in the target, producing a tau lepton. In a set of 203 neutrino interactions, four events were selected, a result consistent with the expected 4.2 τ decays, and the Poisson probability of the background fluctuation to the signal level was 4×10^{-4}. Two types of τ processes were recorded in the selected events, shown in Figure 5:

$$\tau \to h + \nu_\tau + X$$

$$\tau \to e + \nu_\tau + \nu_e.$$

These results confirmed the existence of ν_τ as a partner of the τ lepton.

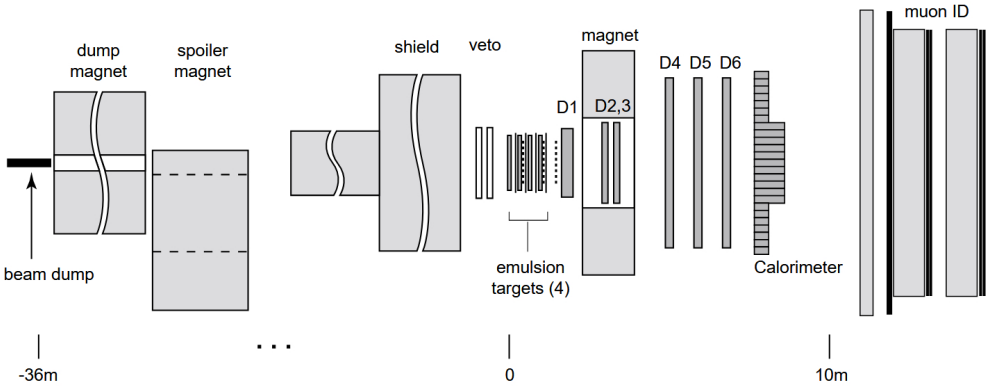

Figure 4: Schematic representation of the DONUT experiment.

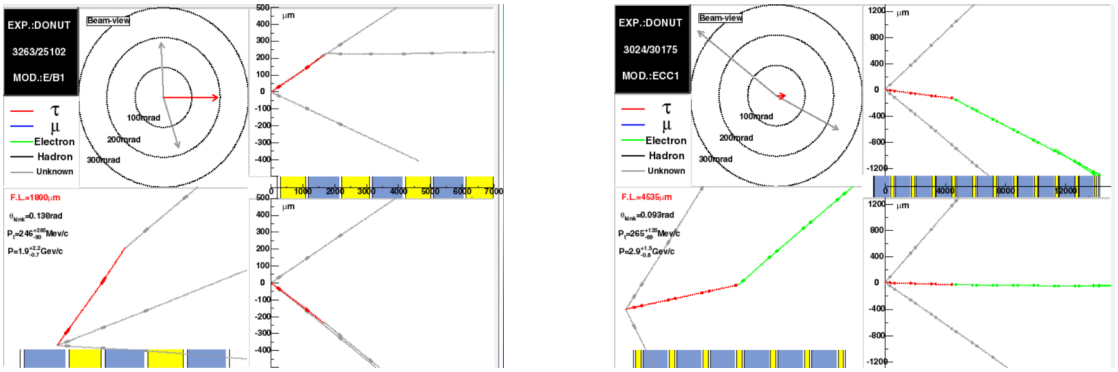

(a) τ decay into hadrons.

(b) τ decay into an electron.

Figure 5: Events recorded in the DONUT detector. (a): The ν_τ interacts with a nucleon in the steel layer producing a τ, which travels to the following steel sheet where it forms an unknown hadron. In the bottom left image three product tracks are clearly visible; however, in the top right picture only two can be seen, signalling that τ and hadron tracks are collinear. (b): The ν_τ interacts with a nucleon in the steel layer, producing a τ, which is identified by locating its kink and observing an electron showering in the emulsion-fibre target.

1.3 Two-component neutrino theory

The two-component theory of the neutrino is the theoretical framework which ultimately placed the neutrino inside the Standard Model of particle physics (better described in Section 1.4).

In order to describe relativistic particles with spin $s = \frac{1}{2}$, in 1928 Dirac proposed his equation:

$$H\psi = (\boldsymbol{\alpha} \cdot \mathbf{p} + \beta m)\psi, \tag{1}$$

or, in its covariant form

$$(i\gamma^\mu \partial_\mu - m)\psi(x) = 0. \tag{2}$$

Here, ψ is the four-component Dirac spinor

$$\psi(x) = \begin{pmatrix} \psi_1 \\ \psi_2 \\ \psi_3 \\ \psi_4 \end{pmatrix}. \tag{3}$$

In Eq. 1, H is the Hamiltonian, $\boldsymbol{\alpha} = (\alpha^1, \alpha^2, \alpha^3)$ and β are 4×4 matrices, $\mathbf{p}$ is the momentum operator, and m is the rest mass of the particle. In the covariant form of the equation (Eq. 2), γ^μ are the Dirac gamma matrices.

After Dirac's proposal, Weyl introduced two-component spinors in order to find Lorentz-invariant equations for the two-component wave functions. For a massless

particle he found two equations, one for left-handed and one for right-handed two-component spinors:

$$i\gamma^\mu \partial_\mu \psi_L(x) = 0, \quad i\gamma^\mu \partial_\mu \psi_R(x) = 0. \tag{4}$$

His theory was initially rejected, since the equations violated parity conservation, which was believed to be a law of nature.

Soon after the first detection of neutrinos, it was discovered in the Wu experiment [12] that weak processes do not conserve parity. Consequently, Landau [13], Salam [14], Lee and Yang [15] proposed the theory of the two-component neutrino. Despite using different arguments in favour of such theory, they all assumed that the neutrino is a massless particle, distinct from its antiparticle, the parity is not conserved in its interactions, and the helicity, which is the projection of the spin on the momentum direction, is -1 for the neutrino and +1 for the antineutrino.

Experimental proof came from Goldhaber, Grodzins and Sunyar in 1958 measuring the neutrino helicity from the analysis of circular polarisation and the resonant scattering of γ rays in europium decay by orbital electron capture [16]. Europium decays by allowed orbital electron capture to the samarium excited state, with the emission of a neutrino:

$$e^- + {}^{152}Eu(J=0) \rightarrow {}^{152}Sm^*(J=1) + \nu_e \ .$$

The excited samarium recoils with a momentum equal and opposite to that of the neutrino because of angular and linear momentum conservation. Therefore, a measurement of the direction of the ${}^{152}Sm^*$ determines the neutrino direction. Considering the initial spins, the conservation of angular momentum also requires that the ${}^{152}Sm^*$ spin is in a direction opposite to that of the neutrino and their helicity is the same. The polarised samarium atom then emits a 960 keV γ ray in the opposite direction of the neutrino and with same helicity, returning to the ground state:

$${}^{152}Sm^*(J=1) \rightarrow {}^{152}Sm(J=0) + \gamma \ .$$

Figure 6 shows the directions of emission of the γ ray in relation to the neutrino helicity. The conditions necessary for resonant scattering are best fulfilled for the photons emitted opposite to the neutrino, thus in the direction of the recoil.

The experimental setup is shown in Figure 7. The ${}^{152}Eu$ source was inserted inside an electromagnet whose field was reversed every three minutes, thus inverting the orientation of the nuclear spins. The γ rays passing through the magnet were resonant-scattered on samarium and detected in a scintillation counter. The circular polarisation was determined by the counting rate, consequently allowing the measurement of the photon helicity, which was found to be negative. Therefore, the neutrino emitted in the orbital electron capture had negative helicity as well.

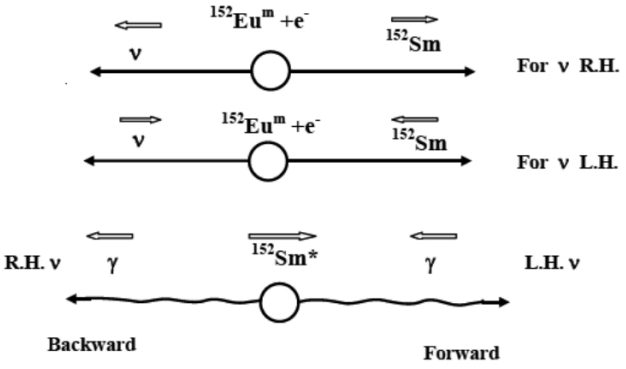

Figure 6: Possible directions of emission of the γ ray. The solid arrows represent the direction of motion and the hollowed arrows represent the spin direction. From top: spin arrangements in the electron capture in the case of right handed ν; spin arrangements in the electron capture in the case of left handed ν; γ emission in the two possible neutrino helicity states [17].

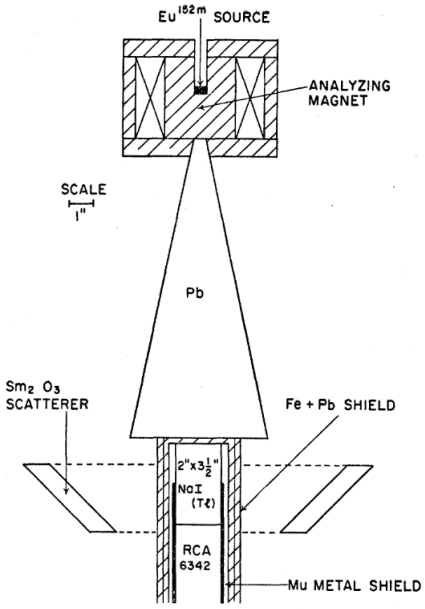

Figure 7: Experimental setup for measuring the circular polarisation of resonant scattered γ rays.

1.4 Neutrinos in the Standard Model

The Standard Model (SM) is a comprehensive theory to classify all elementary particles and describe three of the four fundamental interactions. It was built as a result of theoretical principles and various experiments throughout the XX century, and it is based on a QFD (Quantum FlavourDynamics) gauge theory for the electroweak interaction and a QCD (Quantum ChromoDynamics) gauge theory for the strong interaction. The electroweak unification is described by the Glashow-Weinberg-Salam model (GWS) [18, 19, 20], which includes the electromagnetic and weak interactions.

In the SM particles are divided into bosons and fermions. There are twelve gauge bosons, with spin $s = 1$, which mediate three fundamental forces (photon for the electromagnetic interaction, $W^{\pm}$ and Z^0 for the weak interaction, and eight gluons for the strong interaction) and one scalar boson, with spin $s = 0$, which gives masses to the other particles (Higgs boson). Figure 8 summarises the elementary particles present in the SM. The twelve fermions are leptons and quarks and can be grouped into three generations. They have similar properties but very different masses, which increase with each generation.

In the SM neutrinos are described as left-handed, massless neutral fermions, and they only interact with matter through the weak force. They are part of the

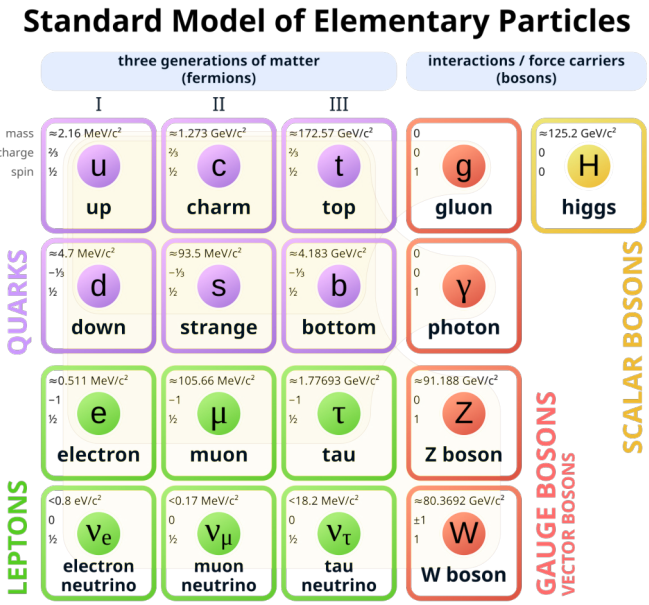

Figure 8: Fundamental particles of the Standard Model. The masses of the particles are as of 2024.

three lepton doublets

$$\begin{pmatrix}\nu_e\\ e^-\end{pmatrix}_L,\ \begin{pmatrix}\nu_\mu\\ \mu^-\end{pmatrix}_L,\ \begin{pmatrix}\nu_\tau\\ \tau^-\end{pmatrix}_L \tag{5}$$

where L stands for the left-handed component of the leptons.

1.4.1 Weak Interactions

Weak interactions are unified with electromagnetic interactions by the GWS model with gauge group $SU(2)_W \times U(1)_Y$. The local gauge symmetry gives rise to the gauge fields $W_\mu^{(1,2,3)}$ associated with $SU(2)_W$ and the gauge field B_μ associated with $U(1)_Y$. The physical bosons of the electroweak interactions, $W^\pm, Z^0$, and photon, are defined as a combination of the four gauge bosons [21]:

$$W_\mu^\pm = \frac{1}{\sqrt{2}}(W_\mu^{(1)} \mp iW_\mu^{(2)}), \tag{6}$$

$$A_\mu = +B_\mu \cos\theta_W + W_\mu^{(3)} \sin\theta_W, \tag{7}$$

$$Z_\mu = -B_\mu \sin\theta_W + W_\mu^{(3)} \cos\theta_W. \tag{8}$$

θ_W is the Weinberg mixing angle and it relates the electromagnetic coupling e to the weak and hypercharge couplings $g,\ g'$.

Neutrinos can interact through the exchange of the mediators of the weak interaction. Depending on the nature of the physical boson, it is possible to distinguish between charged and neutral-current interactions: the massive bosons $W^\pm$ mediate the charged-current weak interactions and couple neutrinos and their corresponding charged leptons; the massive boson Z^0 mediates the neutral-current weak interactions and couples neutrinos among themselves. Charged-current interactions (CC) and neutral-current interactions (NC) are described by the Lagrangian terms [22]:

$$-\mathcal{L}_{\rm CC} = \frac{g}{\sqrt{2}} \sum_{\ell=e,\mu,\tau} \overline{\nu}_{L\ell}\gamma^\mu \ell_L^- W_\mu^\dagger + \text{h.c.}, \tag{9}$$

$$-\mathcal{L}_{\rm NC} = \frac{g}{2\cos\theta_W} \sum_{\ell=e,\mu,\tau} \overline{\nu}_{L\ell}\gamma^\mu \nu_{L\ell} Z_\mu^0. \tag{10}$$

1.4.2 The Brout-Einglert-Higgs mechanism and neutrino masses

Due to the required invariance of the Lagrangian under local gauge transformations, there are no mass terms for fermions and bosons in the Lagrangian of the SM. The mechanism behind the mass generation is the Brout-Englert-Higgs mechanism [23,

24, 25], based on the phenomenon of spontaneous symmetry breaking (SSB). In this process, the Lagrangian remains symmetric, but the states with lowest energy (*vacuum states*) do not exhibit such symmetry.

It is possible to introduce a new field associated to a scalar potential preserving the gauge symmetry and making the vacuum state not invariant under it [21]. In the minimal Higgs model there is a complex scalar field transforming as an $SU(2)_L$ doublet:

$$\phi(x) = \begin{pmatrix} \phi^+ \\ \phi^0 \end{pmatrix} = \frac{1}{\sqrt{2}} \begin{pmatrix} \phi_1 + i\phi_2 \\ \phi_3 + i\phi_4 \end{pmatrix}. \tag{11}$$

In order to generate the masses of the electroweak gauge bosons, one of the scalar fields must be neutral (ϕ^0) and the other must be charged (ϕ^+ and $(\phi^+)^* = \phi^-$). Since the photon is required to remain massless, the minimum of the potential must correspond to a non-zero vacuum expectation value only of ϕ^0. Expanding around the vacuum expectation value v, and writing the Higgs field as $h(x)$, the Higgs doublet can be written as:

$$\phi(x) = \frac{1}{\sqrt{2}} \begin{pmatrix} 0 \\ v + h(x) \end{pmatrix}. \tag{12}$$

The Higgs mechanism can also be used to generate the masses of fermions. The fermion mass term

$$-m\overline{\psi}\psi = -m(\overline{\psi}_R\psi_L + \overline{\psi}_L\psi_R) \tag{13}$$

is not invariant under the $SU(2)_L \times U(1)_Y$ gauge symmetry, and therefore cannot be present in the Lagrangian of the SM. This gauge symmetry is satisfied by a Lagrangian term of the form $-g_f(\overline{L}\phi R + \overline{R}\phi^\dagger L)$, where L and R are the left-handed doublet and the corresponding right-handed singlet of fermion fields and g_f is a coupling constant. For leptons, this term corresponds to:

$$\mathcal{L}_\ell = -g_\ell \left[\begin{pmatrix} \overline{\nu}_\ell & \overline{\ell} \end{pmatrix}_L \begin{pmatrix} \phi^+ \\ \phi^0 \end{pmatrix} \ell_R + \overline{\ell}_R \begin{pmatrix} \phi^{+*} & \phi^{0*} \end{pmatrix} \begin{pmatrix} \nu_\ell \\ \ell \end{pmatrix}_L \right], \tag{14}$$

where $\ell = e, \mu, \tau$. Substituting Eq. 12, the Lagrangian term in Eq. 14 becomes

$$\mathcal{L}_\ell = -\frac{g_\ell}{\sqrt{2}} v(\overline{\ell}_L\ell_R + \overline{\ell}_R\ell_L) - \frac{g_\ell}{\sqrt{2}} h(\overline{\ell}_L\ell_R + \overline{\ell}_R\ell_L). \tag{15}$$

The coupling constant of fermions to the Higgs field g_f is called the Yukawa coupling and it is a fundamental parameter of the SM, related to the fermion f mass as

$$g_f = \sqrt{2}\frac{m_f}{v}, \tag{16}$$

where $v = 246$ GeV.

The non-zero vacuum expectation value occurs only in the lower component of the Higgs doublet; therefore, masses can be generated only for fermions in the lower components of $SU(2)_L$ doublets. While the issue is resolved for quarks by introducing the conjugate Higgs doublet ϕ_c, the same construction cannot be applied to neutrinos, since right-handed neutrino fields are not included in the SM. Furthermore, even if neutrino masses were generated through the Higgs mechanism, the Yukawa couplings would be of order $\lesssim 10^{-12}$, whereas for the charged fermions they are of the order of 1. These arguments suggest the existence of a physical process beyond the SM which generates neutrino masses.

1.5 Neutrino cross sections

As described in the previous section, neutrino reactions with matter fall in the electroweak interactions model. Experiments investigate these interactions covering a wide energy range, shown in Figure 9 [26].

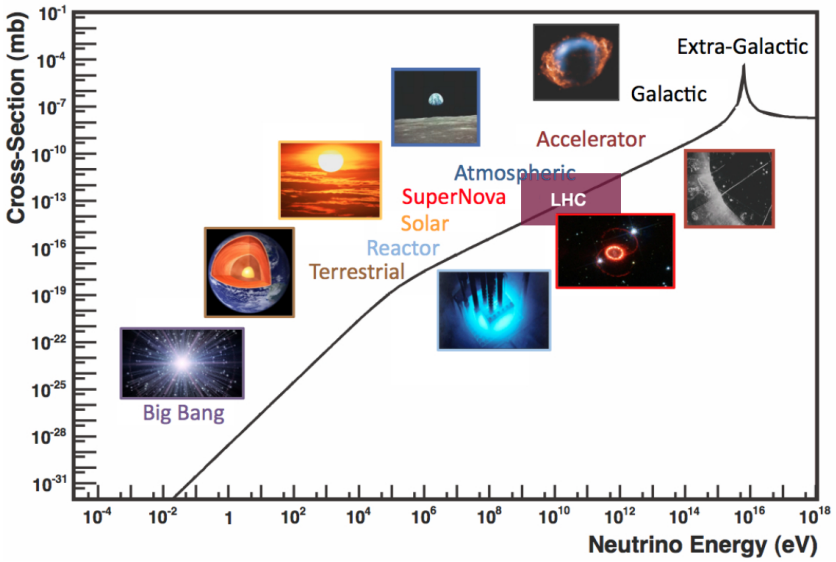

Figure 9: Neutrino sources across decades of energy. The electroweak cross section for $\overline{\nu}_e e^- \to \overline{\nu}_e e^-$ scattering on free electrons as a function of neutrino energy (for a massless neutrino) is shown for comparison. The peak at 10^{16} eV is due to the W^- resonance. Neutrinos produced at LHC at CERN have energies in the highlighted range.

1.5.1 Threshold-less processes: $E_\nu \sim 0 - 1$ MeV

Such processes can be initiated when neutrinos have zero momentum and they include coherent scattering and neutrino capture.

Coherent scattering This is a neutral-current process in which a neutrino interacts coherently with the nucleus:

$$\nu + A_N^Z \to \nu + A_N^{*Z}.$$

At low energy the cross section should be coherent across all the nucleons present in the nucleus; therefore, it grows as the square of the atomic number A^2. Nevertheless, this process has yet to be observed experimentally, partly due to the small energies of the emitted recoil. Such recoil detection can be carried out at dark matter experiments, and the interaction may be a possible signature of cosmic relic neutrinos.

Neutrino capture on radioactive nuclei This process is similar to the β decay, except the neutrino is interacting with the target nucleus:

$$\nu_e + A_N^Z \to e^- + A_{N-1}^{Z+1}.$$

Also in this case, the reaction has yet to be observed.

1.5.2 Low energy nuclear processes: $E_\nu \sim 1 - 100$ MeV

As the energy of the neutrino increases, it is possible to access the individual nucleons of the target nucleus. Unlike the thresholdless scattering mechanisms, these low energy nuclear processes have been studied in neutrino experiments. The simplest nuclear reaction is antineutrino-proton scattering, known as inverse β decay:

$$\overline{\nu}_e + p \to e^+ + n.$$

As discussed in Section 1.1, the study of this process led to the first experimental observation of the neutrino and it typically involves neutrinos from fission reactors.

1.5.3 Intermediate energy cross sections: $E_\nu \sim 0.1 - 20$ GeV

At these energies, several processes can take place. The final states of these neutrino interactions range from nucleons emission to pions, kaons, and mesons production. They can be classified as elastic and quasi-elastic scattering, resonance production, and deep inelastic scattering (DIS). Cross sections for the charged-current processes are shown in Figure 10.

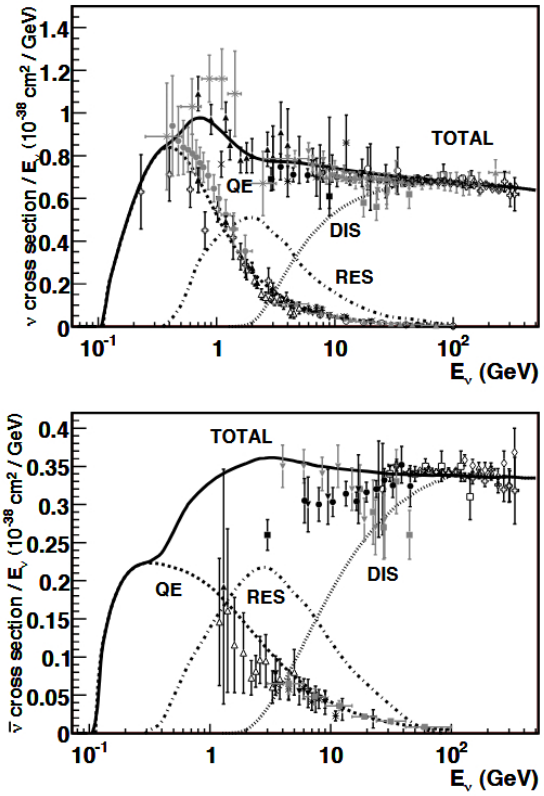

Figure 10: Total neutrino and antineutrino per nucleon charged-current cross section plotted as a function of energy. The plot shows the various intermediate energy processes: quasi-elastic scattering (QE), resonance production (RES), and deep inelastic scattering (DIS). [26].

Elastic and quasi-elastic scattering Neutrinos can elastically scatter off a nucleon freeing one or more nucleons from the target. Quasi-elastic scattering is a charged-current process in which the neutrino has energy lower than ~ 2 GeV. The neutrino scatters off an entire nucleon; in neutrino interactions the target neutron is converted into a proton, whereas in antineutrino interactions the target proton is converted into a neutron:

$$\nu_l + n \to l^- + p,$$
$$\overline{\nu}_l + p \to l^+ + n.$$

Elastic scattering, on the other hand, is a neutral-current process in which neutrinos scatter elastically from nucleons:

$$\nu + p \to \nu + p, \qquad \overline{\nu} + p \to \overline{\nu} + p$$
$$\nu + n \to \nu + n, \qquad \overline{\nu} + n \to \overline{\nu} + n.$$

Resonance production Neutrinos, given enough energy, can excite a target nucleon producing a baryonic resonance that can decay in various mesonic final states. The most common final state includes a nucleon and a single pion:

$$\nu_l + N \to l^- + N^*$$
$$N^* \to \pi + N'.$$

1.5.4 High energy cross sections: $E_\nu \sim 20 - 500$ GeV

At high energies, neutrinos can resolve the internal structure of the target, scattering off individual quarks inside the nucleon (DIS). The neutrino scatters off the quark via the exchange of a virtual W or Z boson producing a hadronic system in the final state. Both NC and CC processes are possible; in the latter a charged lepton is present in the final state along with the hadronic shower:

$$\text{NC} : \nu_l + N \to \nu_l + X, \quad \overline{\nu}_l + N \to \nu_l + X$$
$$\text{CC} : \nu_l + N \to l^- + X, \quad \overline{\nu}_l + N \to l^+ + X$$

An example of CC interaction is shown in Figure 11. The Feynman diagram shows the exchange of a W boson in the DIS of a ν_μ ($\overline{\nu}_\mu$) off a quark in the nucleon. Experiments use DIS events to measure the weak mixing angle, as well as structure functions, inclusive cross sections, and double differential cross sections [26].

1.5.5 Ultra high energy neutrinos: $E_\nu \sim 0.5$ TeV $- 1$ EeV

In the ultra high energy range, a limited amount of data is available. At these energies, various astrophysical objects and mechanisms become accessible, providing

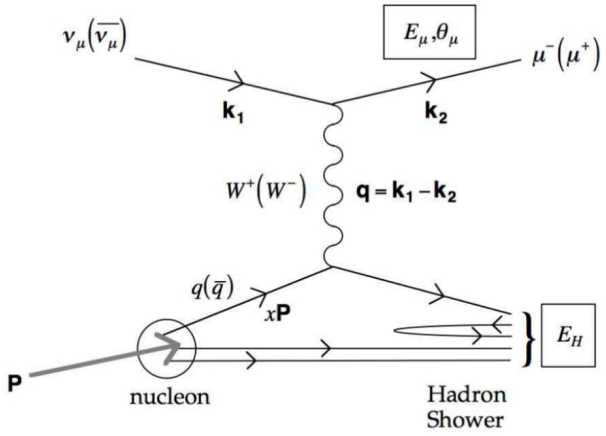

Figure 11: Feynman diagram for a CC $\nu_\mu(\overline{\nu}_\mu)$ DIS process [26].

information complementary to that obtained from electromagnetic or hadronic observations and investigating neutrino astrophysics.

Neutrino-electron scattering is usually sub-dominant to neutrino-nucleus interaction because of its small target mass. However, the neutrino undergoes a resonant enhancement from the formation of an intermediate W boson; the resonance formation takes place at $E_{res} = M_W^2/2m_e = 6.3$ PeV and it is the most prominent process up to 10^{21} eV (Figure 12) [26].

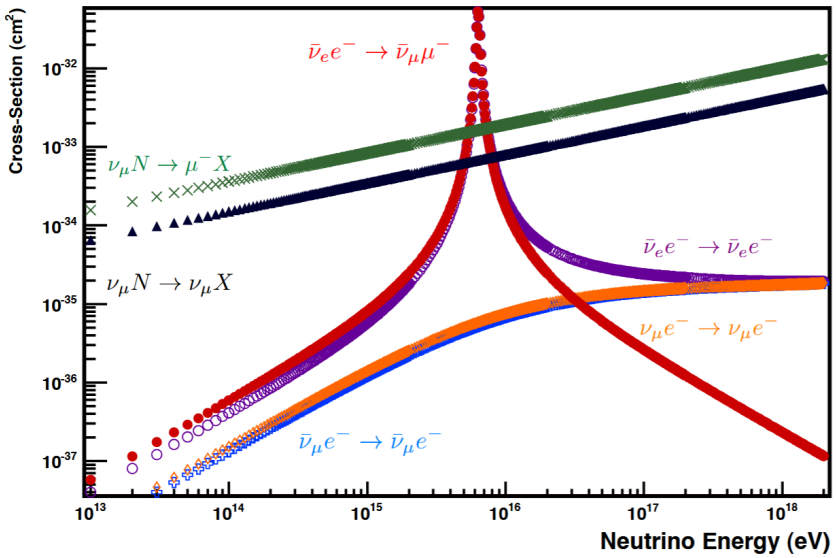

Figure 12: νe and νN scattering cross sections in the ultra-high energy regime. The leptonic W resonance channel is clearly evident (violet and red circles) [26].

1.6 Neutrinos at the Large Hadron Collider

The proton-proton collisions at the LHC, with a center-of-mass energy of 13.6 TeV, generate an intense and strongly-collimated beam of highly-energetic neutrinos and antineutrinos in the forward direction along the collision axis [27]. The energy range of the LHC neutrino beam, from a few hundred GeV to the TeV scale (between the high and ultra-high energy regions described in Sections 1.5.4 and 1.5.5), allows the measurement of neutrino interaction cross sections at energies inaccessible to other experiments, validating neutrino cross section models and providing input for neutrino telescopes. The CERN neutrino program also includes the study of exclusive channels such as the charm associated neutrino interactions $\nu q \to lc$ or the still unobserved beauty associated interactions $\nu q \to lb$. Since the produced neutrino beam includes all three flavours (Section 1.2), a large number of ν_τ events could be collected for precision measurements of its properties and to

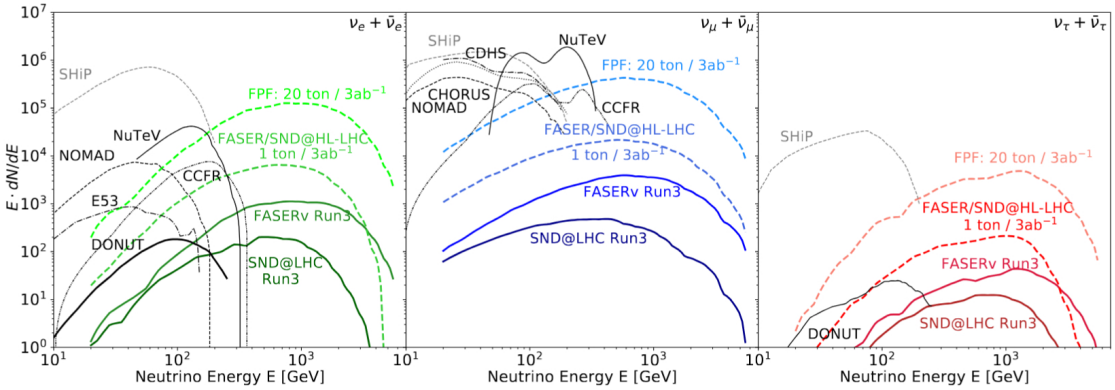

Figure 13: Neutrino yields at existing and proposed collider neutrino experiments. The plots show the expected event rate and energy spectrum of electron (left), muon (middle), and tau (right) neutrinos and antineutrinos [27].

probe lepton flavour universality. Figure 13 shows the expected event rates and energy spectra of existing and proposed collider neutrino experiments compared to previous accelerator experiments. The forward neutrino experiments also probe CC neutrino-nucleus DIS with centre of mass energies in the range $10 - 50$ GeV, establishing the LHC as a neutrino-ion collider in the forward region. High-statistics samples allow the measurement of differential cross sections and the determination of proton and nuclear Parton Distribution Functions (PDFs) with low uncertainties.

The neutrino beam is produced via the decay of light hadrons and charm mesons. The production of light hadrons is described by phenomenological hadronic interaction models. Previously, only neutral pions and neutrons were studied for forward particle measurements at LHC [28, 29]; collider neutrino experiments will add data on the production of charged pions as well as neutral and charged kaons. In contrast, charm mesons production can be modelled using perturbative QCD and they contribute significantly to the tau and electron neutrino flux. Thus, collider neutrino experiments will also contribute to forward charm measurements to study QCD phenomena and provide input for astroparticle physics.

Currently, two neutrino-focused experiments are active at LHC: SND@LHC and FASER (ForwArd Search ExpeRiment).

1.7 Neutrinos beyond the Standard Model

According to the SM, neutrinos are the only massless matter particles; however, the discovery of neutrino oscillations clearly disproves this theory. Furthermore, assuming massive neutrinos, they could be interpreted as Dirac or Majorana particles, and the only way to establish their nature would be the search of

processes violating the total lepton number conservation. In order to introduce a neutrino mass and a mechanism behind its generation, the SM has to be expanded.

1.7.1 Dirac and Majorana neutrinos and neutrino mass

Among the unanswered questions about neutrinos, one of them concerns their nature. Considering the two neutrino fields ν_L and ν_R, after spontaneous symmetry breaking the Dirac mass term is

$$\mathcal{L}^D = -m_D(\overline{\nu}_R\nu_L + \overline{\nu}_L\nu_R), \tag{17}$$

with $m_D = gv/\sqrt{2}$, where g is the Yukawa coupling and v is the vacuum expectation value (Eq. 16) [30]. The invariance of the mass term in Eq. 17 under the global symmetry $U(1)_L$ corresponds to the conservation of the lepton number L. Thus, in the hypothesis of massive Dirac neutrinos, in the SM extended with right-handed neutrinos the total lepton number L is conserved and $L(\nu) = -L(\overline{\nu}) = 1$ [31]. As a result, Dirac neutrinos and antineutrinos are distinguishable. As already mentioned in Section 1.4.2, the generation of Dirac neutrino masses through the Higgs mechanism implies the existence of right-handed neutrinos, known as sterile neutrinos, and fails to explain why the neutrino Yukawa coupling is several orders of magnitude smaller than for other fermions.

In the massless case, the fermionic fields can be described as two-component spinors satisfying the Weyl equations. Majorana showed [32] that a massive neutral fermion can be described by a two-component spinor ψ imposing the condition

$$\psi = \psi^c, \tag{18}$$

where $\psi^c = C\overline{\psi}^T$ is the charge conjugate and

$$\psi = \psi_L + \psi_R \tag{19}$$

is the Majorana field. Using the projector P_R and imposing the Majorana condition, we have

$$\psi_R = P_R\psi = P_R\psi^c = (P_L\psi)^c = \psi_L^c. \tag{20}$$

The Majorana field depends only on the two independent components of ψ_L. Considering the left-handed neutrino field ν_L, it is possible to build the Majorana mass term:

$$\mathcal{L}^M = -\frac{1}{2}m_M(\overline{\nu_L^c}\nu_L + \overline{\nu_L}\nu_L^c). \tag{21}$$

Such Majorana mass term for left-handed neutrinos is not gauge invariant within the SM and therefore suggests physics beyond it. The Majorana condition also implies that neutrino and antineutrino states are not distinct, in contrast to the

Dirac case. Therefore, it is not possible to assign a conserved lepton number. Experimentally, the only way to distinguish between Dirac and Majorana neutrinos is to observe processes violating the conservation of the total lepton number. An example is the neutrinoless double-β decay $(A, Z) \rightarrow (A, Z+2) + 2e^-$, which violates the lepton number conservation by two units.

In the hypothesis of the existence of independent left-handed and right-handed fields, neutrino masses can be described by the Dirac mass term (Eq. 17) and the two Majorana mass terms [30]

$$\mathcal{L}_L^M = -\frac{1}{2} m_L (\overline{\nu_L^c} \nu_L + \overline{\nu_L} \nu_L^c), \quad \mathcal{L}_R^M = -\frac{1}{2} m_R (\overline{\nu_R^c} \nu_R + \overline{\nu_R} \nu_R^c). \tag{22}$$

The total Dirac-Majorana mass term is

$$\mathcal{L}^{D+M} = \mathcal{L}^D + \mathcal{L}_L^M + \mathcal{L}_R^M = -\frac{1}{2} \begin{pmatrix} \overline{\nu_L^c} & \overline{\nu_R} \end{pmatrix} \begin{pmatrix} m_L & m_D \\ m_D & m_R \end{pmatrix} \begin{pmatrix} \nu_L \\ \nu_R^c \end{pmatrix} + h.c., \tag{23}$$

which can be written as

$$\mathcal{L}^{D+M} = \frac{1}{2} \overline{N_L^c} M N_L + h.c., \tag{24}$$

with

$$M = \begin{pmatrix} m_L & m_D \\ m_D & m_R \end{pmatrix}, \quad N_L = \begin{pmatrix} \nu_L \\ \nu_R^c \end{pmatrix}. \tag{25}$$

The masses m_1 and m_2 of the physical neutrino states are the eigenvalues of the mass matrix M:

$$m_{2,1} = \frac{1}{2} \left[m_L + m_R \pm \sqrt{(m_L - m_R)^2 + 4 m_D^2} \right]. \tag{26}$$

In the particular case where $m_L = 0$ and $|m_D| \ll m_R$, the masses $m_{1,2}$ are

$$m_1 \simeq \frac{m_D^2}{m_R} \ll |m_D|, \quad m_2 \simeq m_R. \tag{27}$$

This is known as seesaw mechanism, one of the simplest models to generate the observed small masses of neutrinos. In this model, a heavy state ν_2 with mass m_2 corresponds to a light state ν_1 with mass m_1.

1.7.2 Neutrino mixing and oscillations

The theory of neutrino oscillations was suggested for the first time by Pontecorvo in 1957, although he assumed neutrino-antineutrino oscillations [33]. However, after the discovery of the muon neutrino, Maki, Nakagawa, and Sakata proposed a

model for the oscillation between electron and muon neutrinos [34]. Assuming the existence of three massive neutrinos, neutrino flavour eigenstates ν_α produced in the weak CC interaction of the charged leptons ℓ_α ($\alpha = e, \mu, \tau$) can be written as linear combinations of the mass eigenstates ν_i ($i = 1, 2, 3$):

$$|\nu_\alpha\rangle = \sum_i U_{\alpha i} |\nu_i\rangle , \tag{28}$$

where U is a unitary mixing matrix. Assuming three neutrino flavours and considering the case in which they are Dirac particles, the mixing is described by the 3×3 Pontecorvo-Maki-Nakagawa-Sakata (PMNS) mixing matrix, which depends on three mixing angles θ_{ij} and one Dirac CP phase δ as follows:

$$U = \begin{pmatrix} c_{12}c_{13} & s_{12}c_{13} & s_{13}e^{-i\delta} \\ -s_{12}c_{23} - c_{12}s_{23}s_{13}e^{i\delta} & c_{12}c_{23} - s_{12}s_{23}s_{13}e^{i\delta} & s_{23}c_{13} \\ s_{12}s_{23} - c_{12}c_{23}s_{13}e^{i\delta} & -c_{12}s_{23} - s_{12}c_{23}s_{13}e^{i\delta} & c_{23}c_{13} \end{pmatrix} , \tag{29}$$

where $\delta \in [0, 2\pi]$, $c_{ij} = \cos\theta_{ij}$ and $s_{ij} = \sin\theta_{ij}$.
A physical neutrino, that is a mass eigenstate, can travel a distance L from the source to the detection point and evolve as

$$|\nu_\alpha(t)\rangle = \sum_{i=1} U_{\alpha i} |\nu_i(t)\rangle . \tag{30}$$

Assuming that $|\nu\rangle$ is a plane wave, the evolved state is

$$|\nu_i(t)\rangle = e^{-iE_i t} |\nu_i(t=0)\rangle , \tag{31}$$

where the energy of the neutrino mass eigenstates with mass m_i and momentum $\mathbf{p}_i$ is $E_i = \sqrt{\mathbf{p}_i^2 + m_i^2}$. The amplitude of the neutrino oscillation from a flavour state α to a flavour state β after a time t is

$$\mathcal{A}(\nu_\alpha \to \nu_\beta)(t) = \langle \nu_\beta | \nu_\alpha(t) \rangle = \sum_i U^*_{\alpha i} U_{\beta i} e^{-iE_i t} \tag{32}$$

and the oscillation probability is:

$$P(\nu_\alpha \to \nu_\beta)(t) = |\mathcal{A}(\nu_\alpha \to \nu_\beta)(t)|^2 = \sum_{i,j} U^*_{\alpha i} U_{\beta j} U_{\alpha j} U^*_{\beta i} e^{-i(E_j - E_i)t}. \tag{33}$$

Assuming equal momenta for the different neutrino mass eigenstates and ultrarelativistic neutrinos, the time t can be identified with the travelled distance L in natural units. $(E_j - E_i)$ can be written as

$$(E_j - E_i) \simeq \frac{\Delta m^2_{ij}}{2E}, \tag{34}$$

where $\Delta m^2_{ij} \equiv m^2_i - m^2_j$. Therefore, the oscillation probability is

$$P(\nu_\alpha \to \nu_\beta)(t) = \sum_{i,j} U^*_{\alpha i} U_{\beta j} U_{\alpha j} U^*_{\beta i} \exp\left(- i \frac{\Delta m^2_{ij}}{2E} L \right). \tag{35}$$

Antineutrino mixing can also be described by the PMNS matrix substituting U with its complex conjugate U^*; thus, in general $P(\nu_\alpha \to \nu_\beta)(t) \neq P(\overline{\nu}_\alpha \to \overline{\nu}_\beta)(t)$. However, the difference $P(\nu_\alpha \to \nu_\beta)(t) - P(\overline{\nu}_\alpha \to \overline{\nu}_\beta)(t)$ is small and it has yet to be measured precisely.

Neutrino oscillations were first observed in solar and atmospheric neutrino experiments, such as Homestake [35], GNO [36], SNO [37], and Super-Kamiokande [38]. After their successful results, the phenomenon was further investigated in long-baseline experiments such as KamLAND [39] and Double Chooz [40]. The data from neutrino oscillations experiments allows the measurement of the mass-squared differences, whereas the absolute values of the neutrino masses are still unknown.

In SND@LHC, neutrinos are detected ~ 480 m away from their production point and their energy is ~ 1 TeV. Thus, the ratio

$$\frac{L}{2E} \sim \frac{1}{2000} \tag{36}$$

does not allow flavour oscillation, as the oscillation probability (Eq. 35) would be almost zero.

2 The SND@LHC experiment

SND@LHC is a compact and stand-alone experiment to perform measurements with high-energy neutrinos up to the TeV scale produced at LHC in a hitherto unexplored pseudorapidity region of $7.2 < \eta < 8.4$ [41, 42]. The detector, located in the TI18 tunnel, 480 m downstream of the ATLAS Interaction Point (IP1), is composed of a hybrid system which allows the identification of all three neutrino flavours produced in heavy quark decays and the direct search of Feebly Interacting Particles.

2.1 Physics goals

SND@LHC aims to measure neutrinos in an energy range from hundreds of GeV to few TeV, as shown in Figure 14. Figure 15 shows the energy spectra of neutrinos interacting via charged-current deep inelastic scattering within the SND@LHC acceptance range. The experiment has four main goals in the neutrino analysis: study of charmed hadrons production in proton-proton collisions, test of lepton flavour universality in ν interactions, measurement of the NC/CC ratio, and study neutrino-induced charm production.

2.1.1 Charmed hadron production in *pp* collisions

Charmed hadron production has been studied in other experiments, such as LHCb, in a limited pseudorapidity range [44]. In the η range covered by SND@LHC it is possible to measure the charmed hadron production indirectly through the observation of electron neutrinos and antineutrinos produced in charmed hadron decays. Simulations predict that 10% of the ν_e and $\overline{\nu}_e$ that interact in the detector originate from kaon decays, in particular from K_0s, and have energies below 200 GeV.

The yield of charmed hadrons is estimated in a two-step analysis:

1. Measurement of the $pp \to \nu_e X$ cross section and extrapolation of the energy spectrum and the total number of electron neutrinos and antineutrinos;

2. Derivation of the charmed hadrons yield from the ν_e flux via the estimation of the number of neutrinos and antineutrinos produced in charmed hadrons decays $N(\nu_e + \overline{\nu}_e)^{charm}$. The latter is determined by subtracting the number of neutrinos and antineutrinos produced in kaon decays from the total number of neutrinos and antineutrinos found in the first step.

Neutrinos in the SND@LHC acceptance range are produced by hadrons either lying in the same pseudorapidity range or in adjacent η regions. The number of charmed

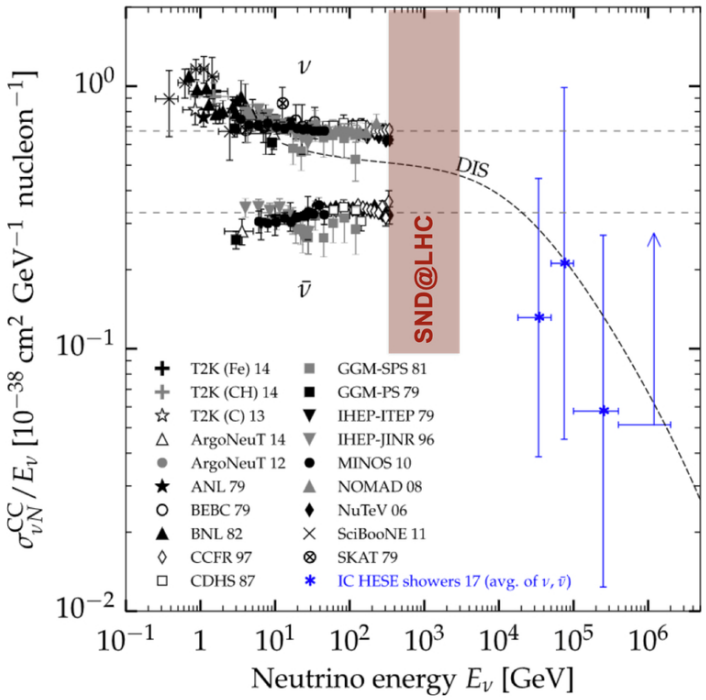

Figure 14: Charged-current neutrino-nucleon cross section measurements [43]. The dashed curve represents the prediction of DIS cross section, averaged between ν and $\overline{\nu}$. The SND@LHC experiment explores the highlighted region from hundreds of GeV to a few TeV.

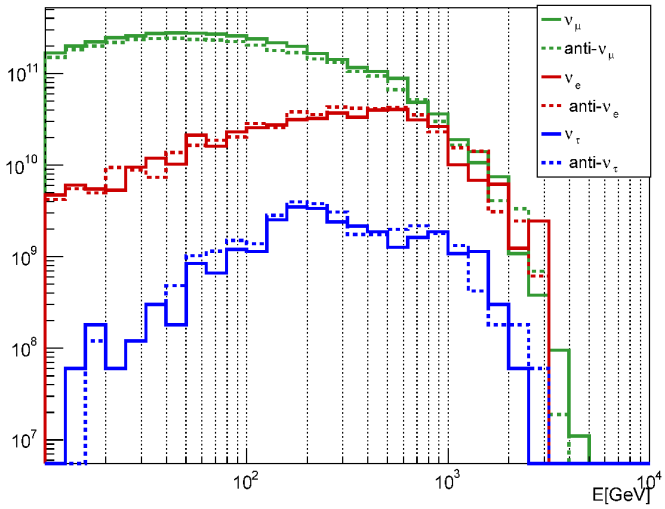

Figure 15: Energy spectrum of the different flavours of incoming neutrinos and antineutrinos as predicted by simulation, normalised to 250 fb^{-1} [41].

hadrons $N(charmed\ hadrons)$ is

$$N(charmed\ hadrons) = N(\nu_e + \overline{\nu}_e)^{charm} \times \frac{f_{AB}}{f_{AC}} \times \frac{1}{Br(c \to \nu_e)}, \tag{37}$$

where $f_{AB} = N_A/N_{A+B}$ is the fraction of ν_e and $\overline{\nu}_e$ coming from charmed hadrons, $f_{AC} = N_A/N_{A+C}$ is the fraction of charmed hadrons that produce ν_e and $\overline{\nu}_e$, and $Br(c \to \nu_e)$ is the branching ratio of charmed hadrons to ν_e. A, B, and C refer to three regions in the two-dimensional phase space of neutrino pseudorapidity (η_{ν_e}) and parent hadron pseudorapidity (η_{hadron}). Region A is the intersection in which both η_{ν_e} and η_{hadron} fall within the ranges under analysis, while in regions B and C only one of the two lies in the desired range (the neutrino for region B and the parent hadron for region C) [41].

2.1.2 Lepton Flavour Universality test in ν interactions

The SND@LHC detector is able to identify all three neutrino flavours, hence to test the Lepton Flavour Universality (LFU) in neutrino interactions.

The experiment detects neutrinos produced in c and b quark decays; ν_τ are produced in $D_s \to \tau\nu_\tau$ and in the subsequent τ decay, whereas ν_e are produced in D^0, D, D_s decays and π and K decays. However, due to their low cross section, the number of ν_e produced in the π and K decays is reduced to 10% and it is possible to assume that both ν_τ and ν_e come from the decay of charmed hadrons. The ν_τ to ν_e ratio R_{13} depends only on the decay branching ratios and on the charm fractions:

$$R_{13} = \frac{N_{\nu_e+\overline{\nu}_e}}{N_{\nu_\tau+\overline{\nu}_\tau}} = \frac{\sum_i \tilde{f}_{c_i} \tilde{Br}(c_i \to \nu_e X)}{\tilde{f}_{D_s} \tilde{Br}(D_s \to \tau\nu_\tau)}, \tag{38}$$

where $\tilde{f}_{c_i}$ are the charmed hadron fractions and $\tilde{Br}(c_i \to \nu_e X)$ are the branching ratios of each charm species. The branching ratio $\tilde{Br}(D_s \to \tau\nu_\tau)$ includes also the contribution from the subsequent τ decay. The tilde symbol indicates that the above quantities are the expected values in the SND@LHC acceptance.

Analogously, also the ν_e to ν_μ ratio R_{12} can be used to test the LFU for $E >$ 600 GeV. The component of the muon neutrino flux coming from π and K decays is dominant at low energies, but it saturates at the level of 35% for $E > 600$ GeV. Considering the uniform contamination of ν_μ and $\overline{\nu}_\mu$ from pions/kaons $\omega_{\pi/k}$, the ratio R_{12} is

$$R_{12} = \frac{N_{\nu_e+\overline{\nu}_e}}{N_{\nu_\mu+\overline{\nu}_\mu}} = \frac{1}{1+\omega_{\pi/k}}. \tag{39}$$

2.1.3 Measurement of the NC/CC ratio

The capability of distinguishing CC and NC interactions offers the possibility to measure the ratio between the NC and CC cross sections. Assuming that the differential ν and $\overline{\nu}$ fluxes as a function of their energy are equal, the ratio is

$$P = \frac{\sum_i \sigma_{NC}^{\nu_i} + \sigma_{NC}^{\overline{\nu}_i}}{\sum_i \sigma_{CC}^{\nu_i} + \sigma_{CC}^{\overline{\nu}_i}}. \tag{40}$$

At LHC energies, the main neutrino interaction is DIS; in this case, the P ratio can be written as a function of the Weinberg angle θ_W [45]:

$$P = \frac{1}{2}\left\{1 - 2\sin^2\theta_W + \frac{20}{9}\sin^2\theta_W - \lambda(1 - 2\sin^2\theta_W)\sin^2\theta_W\right\}, \tag{41}$$

where λ is a correction factor taking into account the unequal number of protons and neutrons in the target [41].

2.1.4 Neutrino-induced charm production

At SND@LHC energies, about 10% of neutrino interactions produce charmed hadrons, allowing the study of charm physics [46, 47]. Feynman diagrams of charm production in charged-current neutrino and antineutrino interactions are shown in Figure 16. In the neutrino interaction, the transition $c \to s$, despite being favoured, is suppressed by the $d \to c$ transition due to the valence d quark in the nucleon. Contrarily, in antineutrino interactions the charmed hadron production selects the anti-strange quark in the nucleon sea quarks.

2.2 Detector environment

The TI18 tunnel, shown in Figure 17, is 280 m long and has a slope of about 15% that levels out as it enters the LHC ring via the UJ18 junction in Sector 12, at about 480 m from IP1. The tunnel was initially constructed for the injection of positrons from the SPS (Super Proton Synchrotron) to the LEP (Large Electron-Positron collider) accelerator. During the preparatory works for the LHC, all but a small section of about 20 m before entering UJ18 has been closed off. At the level of the floor, this section crosses the collision axis of IP1, making the location ideal to explore a high pseudorapidity region not accessible to other LHC experiments. Figure 18 shows the side and top views of the SND@LHC detector inside the tunnel.

2.2.1 Neutrino flux

The neutrino energy versus pseudorapidity phase space in TI18 was studied in simulated proton-proton collisions at $\sqrt{s} = 13$ TeV [48, 49] using PYTHIA 8.2

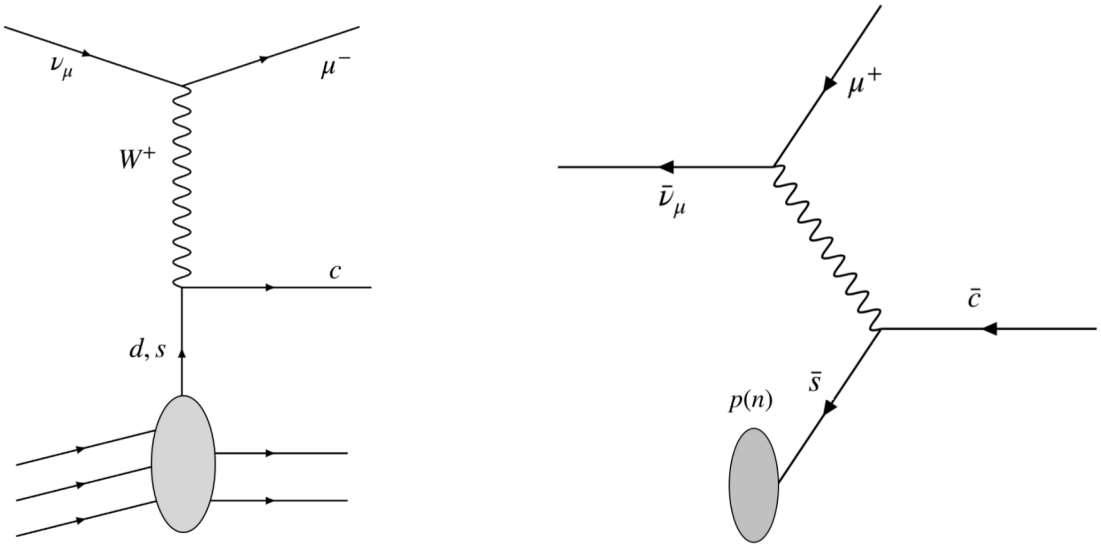

Figure 16: Charm production in neutrino (left) and antineutrino (right) charged-current interactions.

[50]. Figures 19a and 19b show scatter plots of energy versus pseudorapidity $|\eta|$ for neutrinos in pp events with b and c production and in pp events with W production, respectively. PYTHIA events of heavy quark production showed that $\sim 92\%$ of the flux originates from heavy quarks decays; about 5% of the neutrinos are of the τ flavour. Because of the Lorentz boost along the beam axis, their energies can attain the TeV range when $|\eta|$ is 6.5 or larger. Prompt neutrinos from leptonic W decays contribute significantly to the TeV neutrino tail for $4 < |\eta| < 5$, outside the TI18 acceptance range. Thus, a high flux of energetic neutrinos from b and c decays is detected, whereas the contribution from leptonic W decays can be neglected.

Figure 20 shows the neutrino fluxes as a function of η_ν and E_ν within the acceptance of SND@LHC. Although most of ν_e and ν_μ originate from the decay of charmed hadrons, the ν_μ and $\overline{\nu}_\mu$ fluxes are influenced by a low-energy component arising from π and K decays. The average energies are also different, with ν_μ having an average energy of around 150 GeV, while ν_e and ν_τ have an average energy of about 400 GeV.

2.2.2 Backgrounds

Background sources were already studied during the preparation of the FASER technical proposal [51], using both simulations and in situ measurements. Energetic charged particles from IP1 are deviated by the LHC arc optics and they do not

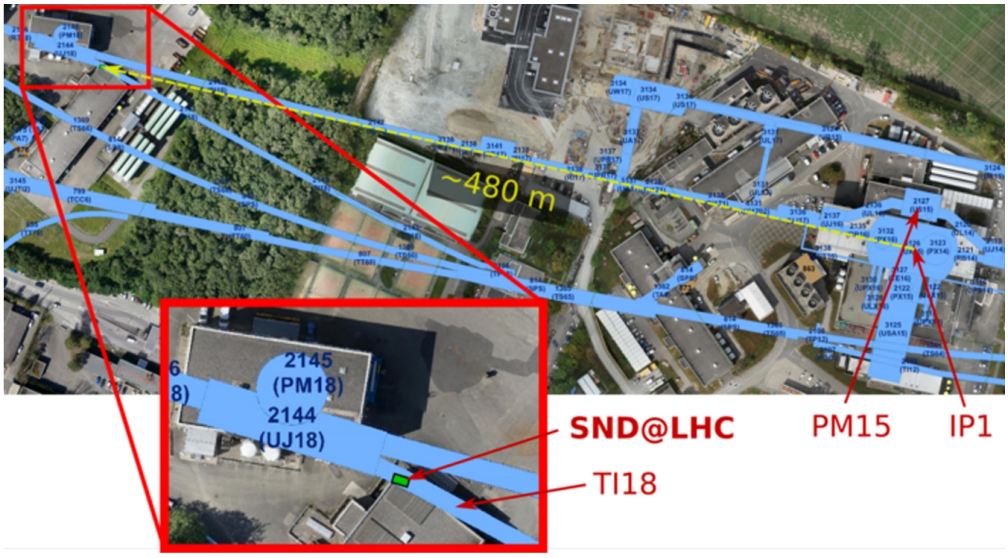

Figure 17: SND@LHC detector location. SND@LHC is located in the TI18 tunnel, accessible from the LHC ring via the UJ18 junction, at 480 m from IP1.

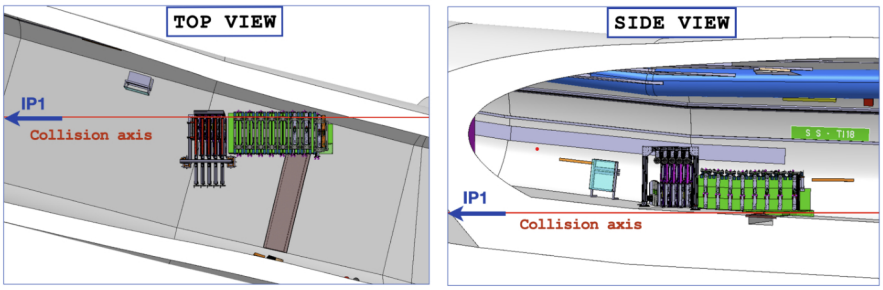

Figure 18: Side and top views of the SND@LHC detector in the TI18 tunnel [42].

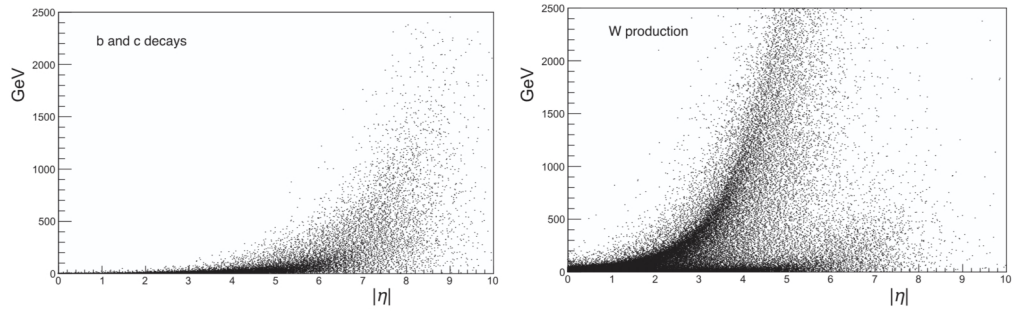

(a) b and c decays. (b) pp events with W production.

Figure 19: Scatter plots of neutrino energy versus pseudorapidity η. All neutrino flavours are included [48].

reach the detector location. The particle flux in TI18 is mainly composed of muons and neutrinos coming from IP1, plus a negligible amount of low energy charged and neutral hadrons [41].

Muons reaching the detector can either enter the fiducial volume without being vetoed and generate showers via bremsstrahlung or DIS, or interact in the surrounding material and produce neutral particles that can mimic neutrino interactions in the target [52]. The expected muon flux in the fiducial area of the detector is estimated to be $\sim 2 \times 10^4$ cm^{-2}/fb^{-1}. This prediction was validated using 2022 data [53].

Muon deep inelastic scattering Deep inelastic muon-nucleon scattering takes place at energy transfers much larger than the binding energy of the nucleon, such that the interaction occurs at parton level and probes the internal structure of the target nucleon. Given an incoming muon with momentum k scattering off a nucleon N with momentum p, the process can be written as:

$$\mu^{\pm}(k) + N(p) \rightarrow \mu^{\pm}(k') + X(p'), \tag{42}$$

where k' is the final muon momentum and X is the final-state hadronic system with total momentum p'. The lowest-order Feynman diagram for the muon-proton deep inelastic scattering is shown in Figure 21.

In addition to the interaction with the tungsten target and the subsequent generation of hadronic showers, muons from IP1 can undergo deep inelastic scattering in the rock upstream and around the SND@LHC detector and generate neutrons and other neutral particles. These neutral hadrons can mimic neutrino neutral current interactions and create a shower in the target. However, events with accompanying charged particles created in the primary muon interaction upstream the detector are rejected by the veto layer, described in Section 2.3.1.

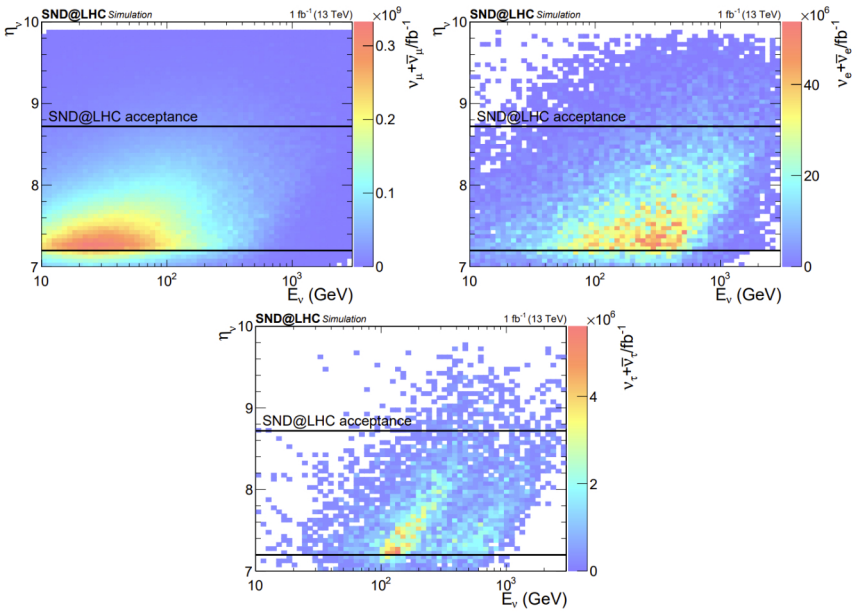

Figure 20: Neutrino and antineutrino flux as a function of energy E_ν and pseudo-rapidity η for muon (left), electron (right), and tau (bottom) neutrinos [41].

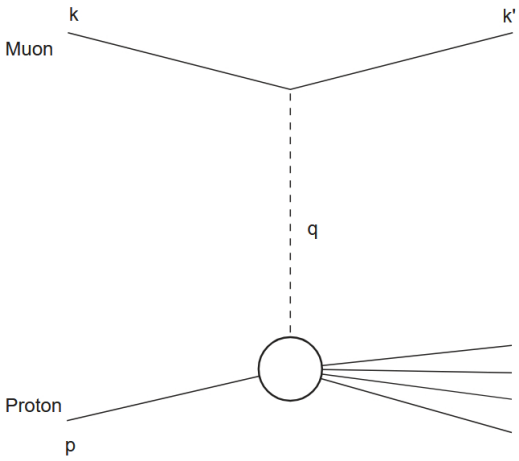

Figure 21: Deep inelastic muon-proton scattering in the lowest order. $q = k - k'$ is the virtual photon and Z boson momentum [54].

2.3 The SND@LHC detector

The detector was designed to identify all neutrino interactions in the available pseudorapidity range. The optimal solution was found to be a hybrid detector that combines nuclear emulsions and electronic detectors. The apparatus, shown in Figure 22, is composed of a target region followed by a hadronic calorimeter and muon identification system [42]. In 2025, Mini Drift Tubes (MiniDTs) were added downstream of the muon system to optimise the reconstruction of muon tracks [55]. Upstream of the target a veto system identifies charged particles. Veto and target region are contained in a 30% borated polyethylene and acrylic box, which acts as a neutron shield for thermal neutrons and as an insulation chamber. The target region comprises five walls of Emulsion Cloud Chambers (ECC) interleaved with Scintillating Fibre (SciFi) planes. The ECC technology makes use of emulsion films, acting as tracking devices, interleaved with tungsten layers acting as the neutrino target. Nuclear emulsions track with sub-micrometric precision all charged particles originating from neutrino interactions. The SciFi modules add time and spatial information in order to disentangle the piled up events and reconstruct tracks between the emulsion walls. Furthermore, they provide energy information and, combined with the tungsten, they act as a sampling electromagnetic calorimeter.

The hadronic calorimeter and muon identification system are located downstream of the target detector and consist of eight iron slabs interleaved with scintillating planes.
Figure 23 shows a schematic layout of the detector front (left) and side (right) view

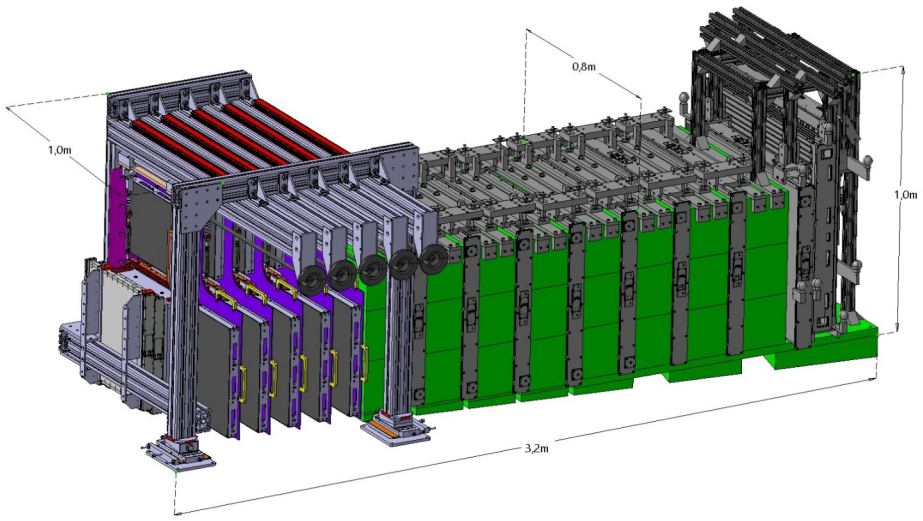

Figure 22: Layout of the SND@LHC experiment.

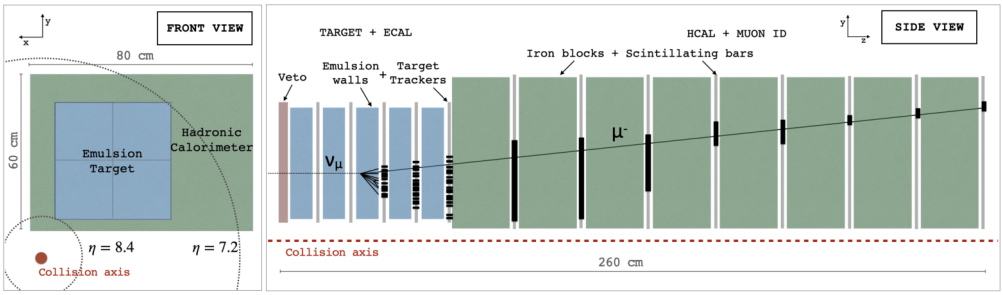

Figure 23: Schematic layout of the SND@LHC detector front view (left) and side view (right) before the 2025 upgrade. The side view includes the display of a ν_μ CC interaction in the target with a hadronic shower [52].

and its position with respect to the collision axis.

2.3.1 Veto system

The veto system is located upstream of the target region and identifies charged particles entering the detector acceptance range. It originally comprised two parallel planes of stacked scintillating bars readout on both sides by silicon photomultipliers (SiPMs). To improve the efficiency of the system [56, 57], during the Year End Technical Stop of 2023-2024 an additional veto station was installed and the entire system was shifted to provide better target coverage, as shown in Figure 24.
Veto 1 and 2 have seven $42 \times 6 \times 1$ cm^3 stacked bars of EJ-200 scintillator aligned horizontally and wrapped in aluminized Mylar foils to ensure opacity and isolate them from light in adjacent bars. Each bar end is read out by eight SiPMs mounted on a printed circuit board (PCB) that covers all seven bars on each end of a plane. The two planes are vertically shifted by 2 cm in order to reduce inefficiencies due to the dead area between bars introduced by the wrapping foils (~ 60 μm) and variations in bar height (~ 250 μm). Veto 3 uses the same technology as the first two planes; however, its bars are aligned vertically and they extend 2 cm above and below the Veto 1 and 2 range, having dimensions $46 \times 6 \times 1$ cm^3. The optimal inefficiency of the veto system was reduced from $(7.8 \pm 2.8) \times 10^{-8}$ in 2022-2023 on a fiducial area corresponding to 64% of the target to $(4.9 \pm 1.9) \times 10^{-9}$ in 2024 with full target coverage [56].

2.3.2 Target and vertex detector

The target consists of five walls of ECC with a transverse size of 384×384 mm^2 divided into four elementary cells called bricks, as shown in Figure 25. Each brick interleaves 57 nuclear emulsion films with a transverse size 192×192 mm^2 and

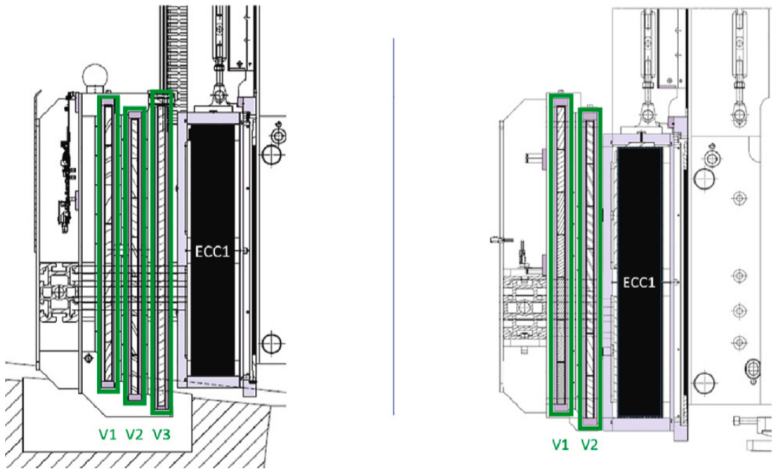

Figure 24: Left: upgraded veto system with a third plane with vertical bars. Right: previous veto system layout with two planes with horizontal bars. [57]

thickness $\sim$ 300 μm with 59 1 mm thick tungsten plates. Because of its high density, tungsten is the ideal passive material to maximise the interaction rate per unit length. Moreover, its small radiation length X_0 ($\sim$ 3.5 mm) allows for good performance in the electromagnetic shower reconstruction in the ECC. The resulting brick has a total thickness of $\sim$ 78 mm, covering $\sim$ 17 X_0, and a mass of 41.4 kg. The total target mass with five walls of 2×2 bricks is $\sim$ 830 kg.
Nuclear emulsion films have two 70 μm-thick sensitive layers on both sides of a transparent 170 μm-thick plastic base. The sensitive layers consist of AgBr crystals with a diameter of 0.2 μm scattered in a gelatin binder. When a charged particle crosses the material, it leaves a latent image, which is enhanced in a chemical process that induces the development of silver clusters with a diameter of 0.6 μm. The track is reconstructed in a single film by connecting the two hits on both sides of the base. As a result of their sub-micrometric spatial resolution and milliradian angular resolution, nuclear emulsions allow for the reconstruction of neutrino event topologies in the bricks with high precision. Figure 26 shows the cross-sectional view of an emulsion and the image of an interaction vertex in the plastic base.

2.3.3 Target tracker and electromagnetic calorimeter

The target tracker system is made of five SciFi planes interleaving the target walls. The SciFi modules consist of blue-emitting scintillating fibres with a diameter of 250 μm and decay time of 2.8 ns arranged in six densely-packed staggered layers, forming 1.35 mm-thick fibre mats (Figure 27). The modules have active area 40×40 cm^2, alternating x and y views. The single particle resolution in one view is of the order of $\sim$ 150 μm and the time resolution for a particle crossing both x

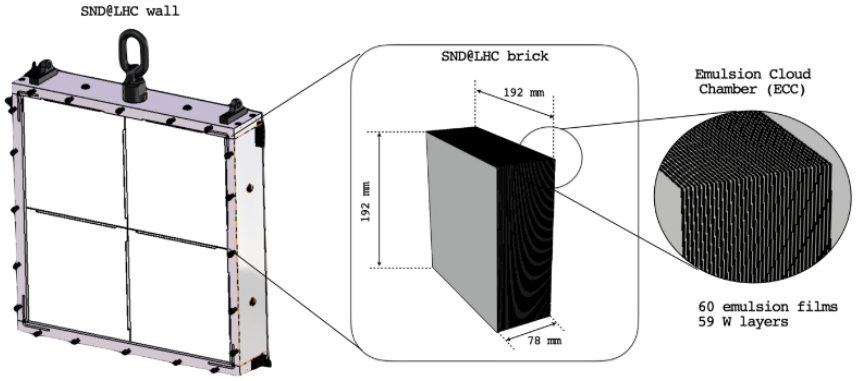

Figure 25: Target wall divided in four Emulsion Cloud Chambers bricks. In the previous configuration 60 emulsion layers were used [42].

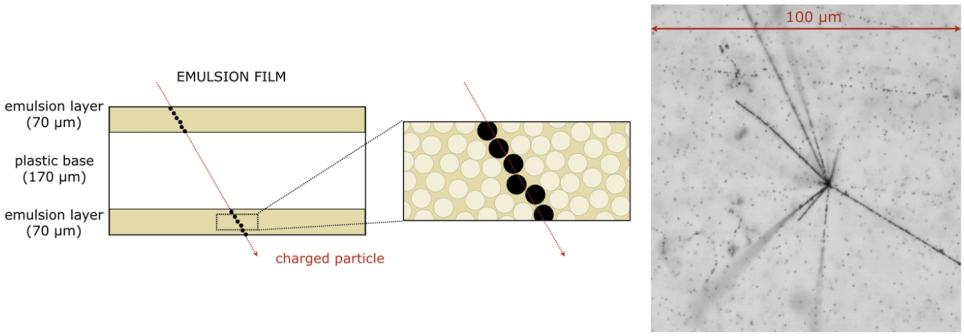

Figure 26: Left: structure of a nuclear emulsion film. The red dashed line shows the trajectory of a charged particle. After the development, silver grains are aligned along the trajectory of the charged particle. Right: Microscope view of an emulsion film. The interaction vertex is visible. [41]

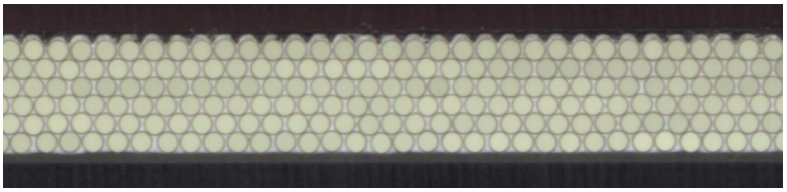

Figure 27: Fibre mat composed of six layers of fibres [42].

and y views of one plane is about 250 ps. The fibre modules are read out by SiPM multichannel arrays optimised for low-intensity detection.
The role of the SciFi system is two-fold: assign a timestamp to neutrino interactions reconstructed in the ECC walls, and provide a measurement of the energy of the electromagnetic showers. The addition of time and spatial information allows the disentanglement of pile-up in the emulsions and the reconstruction of the events between the walls.
SciFi trackers, combined with the emulsion walls, act as a coarse sampling electromagnetic calorimeter which provides the measurement of the electromagnetic showers energy.

2.3.4 Hadronic calorimeter and muon system

The muon system is located downstream the target region. Its primary purpose is to identify muons and, combined with the SciFi, acts as a sampling hadronic calorimeter for the measurement of the energy of hadronic showers.
The system comprises eight layers of scintillating planes interleaved with 20 cm-thick iron slabs, which act as passive material with a total thickness of 9.5 interaction lengths λ_{int}. Considering hadronic showers originating in the target region, the calorimeter covers an average of 11 λ_{int}. The system is divided in two sections: the first five upstream layers (US), and the last three downstream layers (DS). Figure 28 shows the structure of the planes of the two regions.
The five US layers consist of ten horizontally stacked EJ-200 bars with dimensions 1 $cm^3 \times 6$ $cm^3 \times 82.5$ cm^3 wrapped in aluminised Mylar foil. Each bar end is read out by six 6 $mm^2 \times 6$ mm^2 and two 3 $mm^2 \times 3$ mm^2 SiPMs arranged on a custom PCB.
The three DS stations are placed further downstream and they provide the muon position with a resolution higher than 1 cm. Each station consists of two planes of EJ-200 bars wrapped in aluminised Mylar foil: one of 60 horizontal bars (1 $cm^3 \times$ 1 $cm^3 \times 82.5$ cm^3) and one of 60 vertical bars (1 $cm^3 \times 1$ $cm^3 \times 63.5$ cm^3). Each horizontal bar end is read out by one SiPM, whereas vertical bars have one SiPM only on the top edge.

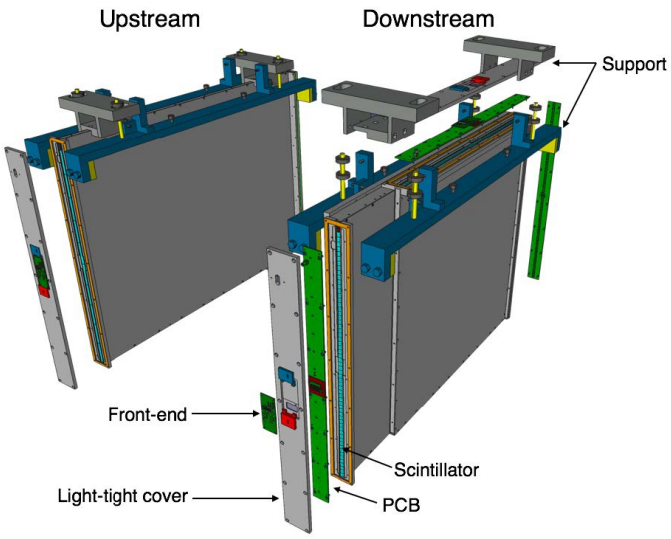

Figure 28: US and DS planes [42].

2.4 Data acquisition

SND@LHC features two types of electronic detector systems: scintillator bars read out by SiPMs in the veto, hadronic calorimeter and muon system, and scintillating fibres read out by SiPMs in the target region. The data acquisition (DAQ) system of the electronic sub-systems is composed of DAQ boards connected to four front-end (FE) boards each, which are based on the TOFPET2, a readout and digitization ASIC for SiPMs [58]. The DAQ boards collect the data digitized by the FE boards and send it to a server. A Trigger Timing Control (TTC) crate allows the DAQ boards to run synchronously receiving the LHC clock and orbiting signals from the Beam Synchronous Timing (BST) system and transmitting them to the DAQ boards. The online system includes two servers: one of them receives data from the DAQ boards, combines them into events, and performs the online processing of the detector data; the other one runs the Experiment Control System (ECS) and other elements of the online monitoring system [42].

2.4.1 Event building

After the transmission of the recorded hits from the DAQ board to the DAQ computer server, event building is performed. The hits are grouped into events based on their timestamp and saved to disk as a ROOT file. The periodic triggers from the TTC system are used by the event building software in the DAQ server to verify that all boards are running synchronously and requesting re-synchronization if this is not the case. Before being saved to disk, data is preliminarily processed

by the DAQ server for data quality monitoring purposes.
The event building process is structured in two main steps, shown in Figure 29. In the first step, hits collected by all boards and with a timestamp within a 25 ns window are grouped into events. The event timestamp corresponds to the timestamp of the earliest hit within the event. In the second step, events are filtered and processed and written to disk. During the processing the noise filtering is performed, which is in turn divided in two additional steps: in the first one, events are required to have a minimum number of DAQ boards that have detected a certain number of hits, eliminating single noise hits; in the second step, the hits are grouped by the plane that generated them, adding requirements on the topology of the events.
The DAQ server writes the recorded data to a local disk. At the end of each run it is stored and can be used for offline reconstruction and data analysis.

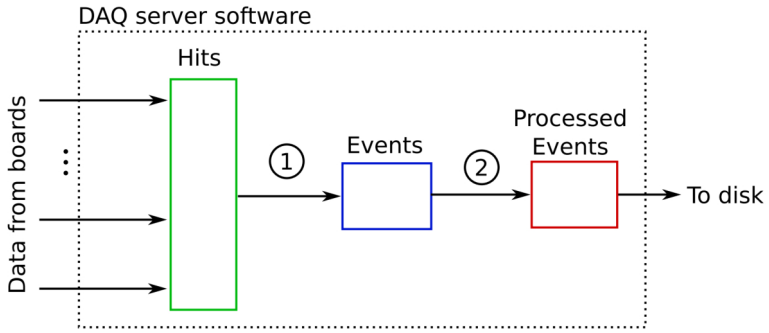

Figure 29: Schematic view of the event builder process [42].

3 Monte Carlo simulation in SND@LHC

Monte Carlo (MC) event generators simulate particle physics processes as they would be observed by an ideal detector. The output of an event generator is in the form of events with the same average behaviour and fluctuations as real data. MC methods are used to explore all relevant variables and ensure randomness in the final events.
Event generators are used for various purposes. Their main applications are:

- to predict the expected number of events;
- to assist the design of a new detector and the optimisation of its performance;
- to support the development of real data analysis strategies for the maximisation of the signal and background separation;
- to estimate detector acceptance corrections to be applied to real data analysis;
- to interpret the experimental observation in terms of an underlying theoretical model.

It should be noted that MC simulations are not a perfect reproduction of reality. A tuning process and a comparison with experimental data are essential to ensure an accurate simulation of the physics processes and detector response.
In SND@LHC, the event simulation is structured in different steps.

1. Primary particle production and transport: FLUKA models the proton-proton collisions at the interaction point and the subsequent transportation of the particles through rock and LHC magnets between IP1 and the detector site.
2. Physics process generation: specific generators simulate the interaction of the primary particles generated with FLUKA within and around the detector geometry. GENIE is used to simulate neutrino interactions, whereas muon interactions are simulated with PYTHIA. These generators determine kinematics and types of secondary interactions.
3. Detector response: the GENIE/PYTHIA simulation output serves as input for GEANT4 for particle transport through the detector.

The output of the simulation chain is then digitized, converting the energy deposition produced into signals in the detector and effectively linking MC information and reconstructed objects used in data analysis. More recently, also a Monte Carlo Event Builder has been implemented to mimic the DAQ Event Builder.

3.1 Physics at the interaction point

The general purpose MC code FLUKA [59, 60] is the reference tool at CERN for the interaction and transport of hadrons, heavy ions, and electromagnetic particles from keV to cosmic ray energies. At LHC, it is used to assist and upgrade the accelerator chain and, for these purposes, it models the geometry of several hundred metres of accelerator portions [41]. As an example, Figure 30 shows a view of the right side of the ATLAS insertion from the experimental cavern up to the TI18 tunnel, as implemented by FLUKA.

In the context of SND@LHC, FLUKA is used to simulate the production of particles at the LHC IP1 and their subsequent propagation to the detector location. To simulate LHC proton-proton collisions, FLUKA uses the DPMJET-III code [61, 62] as event generator. DPMJET is a high-energy hadron-hadron, hadron-nucleus, and nucleus-nucleus interaction model that describes interactions from several GeV per nucleon up to the highest cosmic ray energies. It is based on the Dual Parton Model, which provides the phenomenological description of multiparticle production processes that cannot be described within perturbative QCD. The DPMJET code has been benchmarked against Run 1 physics data, including those of the forward detectors [41]. Moreover, an independent validation is provided by the Beam Loss Monitors (BLM) system, consisting of ionisation chambers that

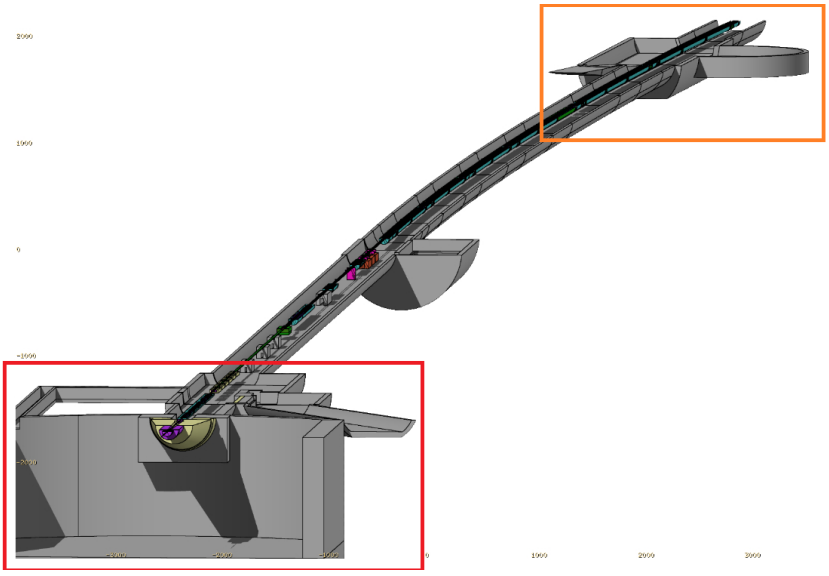

Figure 30: 3D view of the right side of the LHC Point 1 insertion, as modelled in FLUKA. Red: ATLAS detector forward shielding. Orange: arc near the location of the TI18 gallery. The geometry covers a length of about 500 m and includes models of vacuum chambers, absorbents, and magnets [41].

provide measurements of the energy released by the particle showers originating from beam losses and the collision debris.

As discussed in Section 2.2, the particle flux in TI18 is mainly composed of neutrinos and muons from IP1, plus a minor contribution from low energy charged and neutral hadrons. For muons, the FLUKA package takes into account proton-proton interactions at the IP as well as proton interactions with LHC machine elements, including magnetic fields through the trajectory. In MC muon flux studies, the model of the LHC magnetic fields plays an important role, as positively and negatively charged particles can be deflected towards or away from the detector acceptance region. Furthermore, they pass through the beam pipe and machine elements, where the magnetic field is different. The FLUKA particle transport is stopped at a virtual scoring plane with an area of 1.8×1.8 m^2 located about 60 m upstream of the TI18 tunnel. Here, positions and momenta of muons are recorded together with their statistical weight, in order to decouple the muon interactions in rock and concrete from the primary flux of muons produced at the IP and within the LHC machine elements [53]. The FLUKA simulation file contains:

- FLUKA run number;
- FLUKA particle ID;
- Generation number, which reports at what level the particle is created within the decay chain;
- Statistical weight;
- Kinetic energy of the particle in GeV;
- (x, y, z) coordinates of the particle at the scoring plane in cm;
- x and y direction cosines.

In addition, the FLUKA muon simulation accounts for the proton beams crossing angle, which cross in IP1 with a half-angle of 150 μrad, either upward or downward in the vertical plane.

3.2 Propagation throughout SND@LHC

The second stage of the simulation chain is carried out by the SND@LHC Collaboration. The Collaboration software framework provides suitable interfaces for particle guns and event generators, including GENIE [63] for neutrinos, PYTHIA 6 [64] and PYTHIA 8 [65] for other particles, as well as event generators for specific backgrounds. GEANT4 [66] is used for particle transport through the detector.

3.2.1 Neutrino simulation with GENIE

GENIE is a ROOT-based [67] neutrino MC generator which simulates the dominant scattering mechanism in a wide energy range, spanning from MeV to PeV scales. In this range several processes can occur, which can be categorised into nuclear physics models, cross section models, and hadronisation models. The cross section model provides the calculation of the differential and total cross section. During event generation, the total cross section is used together with the flux to determine the energies of interacting neutrinos. The cross sections for specific processes are then used to determine the event kinematics. Neutrinos in the energy range of LHC interact mainly via deep inelastic scattering; in this model the cross sections are computed at fully partonic level ($\nu q \to l q'$) for all sea and valence quarks.

The output unit of an event generation process in GENIE is a "particle", which describes particles and nuclei in the initial, intermediate and final state. These objects contain information including particle ID code, PDG mass, charge, name, information about mother and daughter particles, 4-momentum, 4-position, and other properties. Each particle is also marked with a status code which refers to its position in a time-ordering of the event. All particles are then stored in a dynamic container representing an event. An event provides additional information with event-scope, such as cross section and event weight. Interaction summary information is stored in the "interaction" object. It includes a description of the initial state, the process type and the scattering kinematics.

GENIE uses a flux driver to sample individual neutrinos, assigning flavour, weight, 4-momentum and 4-position (in the detector coordinate system). The neutrino is then propagated towards the detector geometry; GENIE calculates density-weighted path-lengths for all nuclear targets in the geometry and the interaction probability, and decides whether the neutrino should interact. As for the input geometry information, GENIE, starting from the list of target nuclei contained in the detector, computes the density-weighted path-lengths for all nuclear targets, for a trajectory of given 4-momentum and starting 4-position. This allows the calculation of the nuclear scattering probability. A vertex along a trajectory of given 4-momentum and starting 4-position is generated, placing the neutrino interaction vertex within and around the detector geometry.

Finally, the generated events are stored in the ROOT file format.

3.2.2 Muon DIS simulation with PYTHIA

PYTHIA is widely used in high-energy physics for simulating multiparticle production in collisions between single particles. It includes various physics scenarios with more than 200 different subprocesses. The main applications are:

- Fragmentation and hadronization;

- Parton showers;
- Deep inelastic scattering;
- Photon physics;
- Beyond the Standard Model physics.

For the simulation of muon DIS events, SND@LHC uses PYTHIA 6.4, which provides the framework for the generation of the lepton-hadron interactions from the hard scattering level to the final stable state. DIS is treated at leading order as a fermion-fermion interaction between the lepton, which is considered as a point-like particle, and a parton inside the struck hadron, which is described by Parton Distribution Functions. PDFs parametrize the probability of finding a parton i with a fraction x of the hadron momentum when it is probed by a hard scattering with a momentum transfer Q^2. In PYTHIA 6 the hard subprocesses, parton showers, beam remnants, and hadronization are treated separately.

The most general DIS subprocess is

$$f_i f_j \to f_k f_l, \tag{43}$$

where f denotes a general fermion. For this process, contributions from γ, Z^0, and $W^\pm$ exchange are included, as well as the interference between γ and Z^0. In addition, PYTHIA provides the process:

$$q_i f_j \to Q_k f_l, \tag{44}$$

which is equivalent to the previous one for $W^\pm$ exchange only. Here, q_i is the quark in the hadron, while Q_k is a final state heavy quark. In hadron colliders, this process is of interest for the heavy flavour production.

Higher order QCD effects are important at high energies where multiple parton emission can give rise to multijet events or affect the internal properties and the overall structure of the event. Such effects are approximated in PYTHIA by parton showers. Initial-state radiation is generated from the quark before the interaction. At each instant, a parton close to mass-shell inside the hadron can initiate a parton shower which can be described in terms of a tree-like structure, composed of subsequent branches $a \to b\ c$. In each branch one parton becomes increasingly off-shell with a space-like virtuality ($m^2 < 0$), while the other is on-shell with a time-like virtuality ($m^2 > 0$). The cascade continues until all partons are off-shell, before reassembling. Initial-state radiation is simulated using a "backwards" evolution scheme, in which the hard scattering is first selected, and the parton shower that preceded it is reconstructed. Analogously, the final-state radiation is generated from the scattered quark after the hard interaction. Many approaches

can be chosen for the algorithm, including, for example, kinematic reconstruction, matrix-element correction, or in terms of evolution variables. The most common approach in PYTHIA is the mass-ordered `PYSHOW` algorithm, where the evolution variable Q^2 is associated with the squared mass of the branching parton.

The hard scattering between the lepton and a parton of the hadron leaves behind a remnant system which does not take active part in the process nor in the initial-state radiation. If the interacting parton is a valence quark, the nucleon remnant is a diquark composed of the other two spectator quarks. On the other hand, when a sea quark is kicked out ("companion quark"), it leaves behind an antisea parton in the remnant, by flavour conservation. Scattered partons and remnants must be coupled in colours, transverse momenta, and longitudinal momenta. Since in DIS only a single coloured parton is involved in the process, there is a single colour connection and multiple parton interactions do not occur.

Hadronization is modelled using the Lund string fragmentation model. In this model, a colour string connects the struck quark, carrying colour triplet charge, to the beam remnant. As the quark propagates, the string stretches and eventually breaks when the potential energy is high enough, producing quark-antiquark pairs which combine into hadrons.

The main output of the simulation chain is the event record, that includes the complete history of each generated event and information about all involved particles and is stored in the common block `PYJETS`. Each particle represents a row in a table; its components state the nature of the particle, the origin, the present status (fragmented/decayed or not), its momentum, energy and mass, and the space-time position of the production vertex. Some internal PYTHIA routines, such as `PYLIST`, can be used to print or summarize the event record during runtime.

3.2.3 Particle transport with GEANT4

The GENIE/PYTHIA simulation output serves as input for GEANT4 for particle transport through the detector. GEANT4 is a toolkit for simulating the passage of particles through matter. It has a modular and hierarchical structure and covers a wide range of domains, including:

- Geometry and materials;
- Particle interaction in matter;
- Tracking;
- Digitization and hits;
- Visualization and visualization framework;

- User interface.

The toolkit allows the creation of a geometrical model with several components of different shapes and materials and to define sensitive elements that record information (energy deposition) needed to simulate detector responses. The design includes several categories; the top level categories and their relationship are shown in Figure 31. Categories at the bottom of the diagram represent the foundation of the toolkit:

- *Global* covers the system of units, constants, numerics, and random number handling;
- *Material*, *Particle*, *Geometry*, and *Graphical Representations* include the volumes for detector description and the navigation in the geometry model;
- *Intercoms* allows the interaction with GEANT4 through the user interface and the communication between independent modules.

Above these, there are the categories that describe the tracking of the particles and the physical processes they undergo:

- *Track* contains classes for tracks and steps;
- *Processes* uses the tracks in *Tracks* and contains implementations of models of physical interactions; among these processes, *transportation* handles the transport of particles in the geometry model;
- *Tracking* may invoke all these processes and manage their contribution to the evolution of a track's state, additionally providing information in sensitive volumes for hits and digitization;
- *Event* manages the simulation of an event in terms of its tracks;
- *Run* manages collections of events that share a common beam and detector implementation;
- *Readout* allows the handling of pile-up;
- *Visualization*, *Persistency*, and *Interfaces* use all of the above categories and connect to facilities outside the toolkit.

The interface to the external event generators such as GENIE and PYTHIA is provided by the *Event* category. Primary vertices and primary particles are represented by special classes which can be used to interface to the physics generators. The primary particle can represent even particles that cannot be treated by GEANT4,

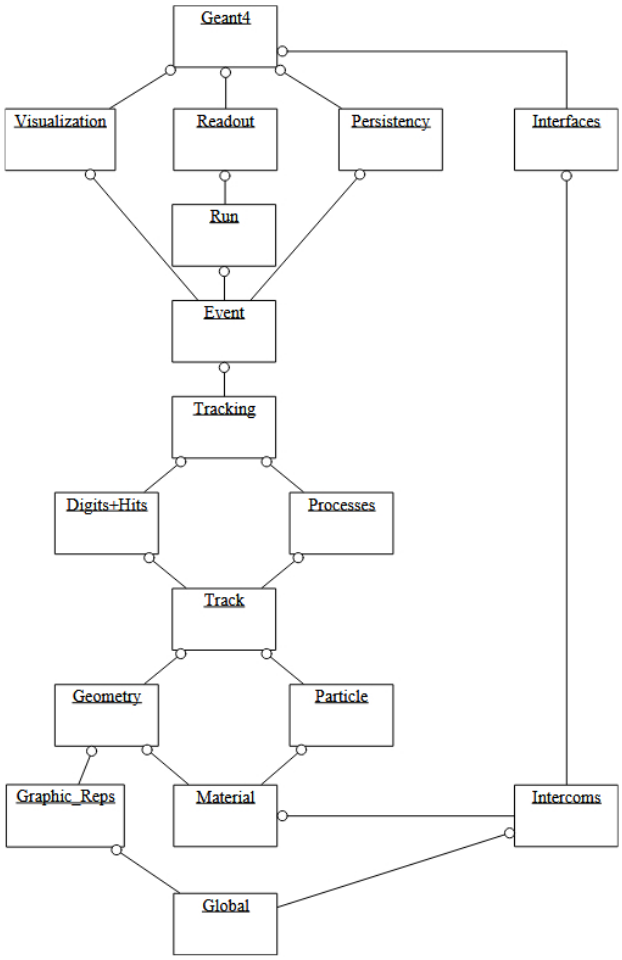

Figure 31: The Top Level Category Diagram of the GEANT4 toolkit [66].

such as gauge bosons, to keep the specific decay chain simulated by the event generator intact. Before processing the event, primary vertices and primary particles are contained in the `G4Event` class, which represents an event. After processing, it has hits and trajectories for the recording of the simulation truth.

The *Geometry* category allows the description of the geometrical structure and the propagation of particles through it. It is possible to distinguish between logical and physical volume. A logical volume represents a detector element of a certain shape that can hold other volumes inside it and it contains information that does not depend on the physical position in the detector, such as material and sensitivity. A physical volume, on the other hand, represents the spatial positioning of the logical volume.

In GEANT4, the transportation process moves particles in steps determined by physics processes and detector geometry. The `G4TrackingManager` orchestrates the interaction between the event and the tracks,while the `G4SteppingManager` steers the individual steps. The particles are represented as objects of the `G4Track` class holding information about each step, such as current position, time since the start of the stepping, and the identification of the geometrical volume where the particle is.

In SND@LHC, the detector geometry is implemented using the ROOT `TGeo` package and used in the simulation by GEANT4. A model of the detector, the neutron shield, and the surrounding tunnel is shown in Figure 32. Electronic detectors and emulsion films are implemented as sensitive volumes. Moreover, for electronic detectors the full granularity is implemented, from scintillator bars to single scintillating fibres. The GEANT4 simulation stops with the deposition of energy in the sensitive detectors.

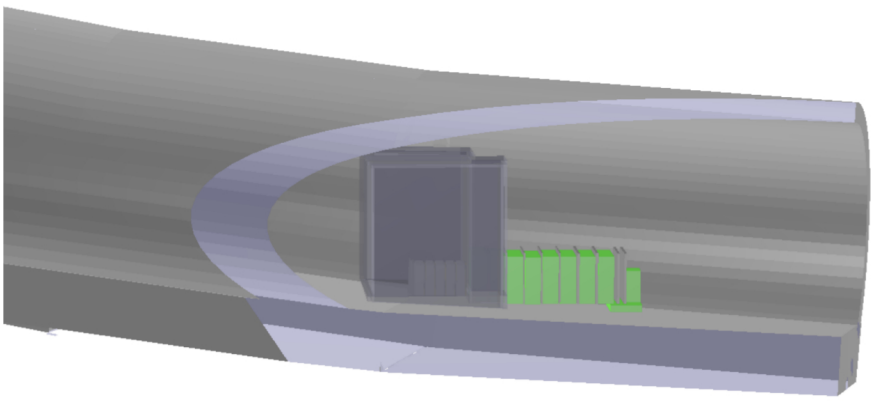

Figure 32: The SND@LHC detector layout and the TI18 tunnel geometry as implemented in the GEANT4 simulation [42].

3.3 Digitization

Digitization converts the energy depositions produced in the simulation into signals in the detector. Hence, it represents an interface between MC truth information and reconstructed objects used in data analysis.

The offline software framework `sndsw` [68] is based on `FairShip` [69] and `FairRoot` [70]. Particles simulated in the MC simulation produce `FairRoot` objects when interacting in the SND@LHC detector. Each simulated particle is represented by an `MCTrack`, which contains information such as particle identification code, information about the mother track, 4-momentum, position of the production vertex, and energy. When a particle crosses the sensitive volume of the detector and deposits energy, a corresponding `MCPoint` is created. It records the position of the energy deposition, the amount of energy deposited, the index of the `MCTrack`, and the detector identifier. Depending on the electronic detector, in `sndsw` a MC point can be represented as a `ScifiPoint`, if the energy deposition is in the SciFi system (Section 2.3.3), or as a `MuFilterPoint`, if the energy deposition is in the Muon Filter system, composed by Veto, Upstream System, and Downstream System (Sections 2.3.1 and 2.3.4).
The digitization is implemented in `sndsw` through a dedicated digitization task, which operates event-by-event.

In the SciFi tracker, individual `ScifiPoint` objects represent energy loss in the scintillating fibres. In the digitization algorithm, each energy deposit is converted into scintillation light; these photons are then converted into photoelectrons by the SiPM pixels, with the average number of photoelectrons taken to be proportional to the deposited energy. The conversion factor corresponds to 0.16 photoelectrons per keV of deposited energy. Since scintillation light propagates along the fibre towards the SiPM readout, the light yield is attenuated depending on the distance between the ScifiPoint and the SiPM. To account for the finite dynamic range of the SiPMs, a saturation model is applied, which limits the number of fired pixels for large light yield. The resulting number of fired pixels is then converted into a digitized charge using a linear calibration. A minimum signal threshold is applied so that only signals exceeding a certain number of photoelectrons are considered valid hits. The nominal threshold is at 3.5 photoelectrons. During the digitization process, also timing information is assigned to the hits. For each MC point, the light propagation time from its position to the SiPM is computed using a constant signal speed. The earliest arrival time among all contributing points is selected as the reference time for the hit. The time is smeared with a Gaussian resolution to emulate the detector behaviour. At the end of the digitization process, a `Digi_ScifiHit` object is produced, which corresponds to the response of a single SiPM channel. Moreover, for each hit the contributing MC points are linked using the `Digi_ScifiHit2MCPoints` objects. They include a weight equal to the fraction

of the total deposited energy contributed by the corresponding MC point.

The Muon Filter, on the other hand, consists of thick scintillator bars. For each bar, all energy depositions recorded as `MuFilterPoint` within the bar are combined during the digitization. Similarly to the SciFi case, the light produced by each deposition is attenuated according to the distance between the MC point and the readout ends. Detector-specific calibration constants are applied to convert the summed energy deposits into digitized signal for each channel. However, in this case, no saturation model is applied at pixel level and the signal is assumed to scale linearly with the deposited energy. As for the timing information, it is derived from the propagation of the scintillation light along the bar and for each MC point the arrival times at the two ends of the bar are calculated using the propagation speeds. The earliest arrival time on each side is selected as the reference time for the hit and it is smeared with a Gaussian time resolution. The digitization process produces a `Digi_MuFilterHit` object, which represents the response of a single scintillator bar. It is important to underline that, in the current digitization process, if a hit is created in the Muon Filter all SiPMs coupled to that bar are considered to be fired simultaneously. As in the SciFi digitization, `Digi_MuFilterHits2MCPoints` link digitized hits and the contributing MC points.

3.4 Monte Carlo Event Builder

To better simulate the detector response, the Monte Carlo Event Builder algorithm [71] was developed to mimic the DAQ Event Builder, described in Section 2.4.1. The MC points generated in each simulated event are grouped in 25 ns time intervals. In the event builder algorithm, all MC points in the SciFi and Muon Filter systems are sorted chronologically based on the time they reach the readout. The earliest time across both systems is used as a reference for the construction of the 25 ns time windows in which all subsequent MC points are grouped. As for the MC track information, it is extracted and stored only in the case of those with an energy exceeding a 100 MeV threshold. Throughout the event building process, the original event header is kept, linking entries in the new output file and their corresponding events in the original simulation and allowing an event-by-event comparison and validation against the initial simulation data.

As in the DAQ case, the MC Event Builder includes a two-layer noise filter applied to each 25 ns window. In the Fast Noise Filter, the requirements are the minimum number of DAQ boards and the minimum total number of hits, whereas in the Advanced Noise Filter the requirement is the minimum number of planes. Figure 33 reports the requirements for the two cases.

Criteria	VETO	SciFi	US	DS
Minimum DAQ Boards	-1	3	5	2
Minimum total hits	5	10	-1	2

(a) Fast Noise Filter.

Criteria	VETO	SciFi	US	DS
Minimum planes	1	4/5	2/5	2/4
Minimum total hits	-1	-1	-1	-1

(b) Advanced Noise Filter.

Figure 33: Fast (a) and Advanced (b) Noise Filter criteria. The value -1 means that the requirement is not being used [71].

4 Characterization of muon deep inelastic scattering events

4.1 Physics case

In SND@LHC the dominant CC process that occurs for muon neutrinos is deep inelastic scattering (CCDIS), given the high energy of neutrinos in the detector acceptance range. The signature of these interactions includes a muon track in the muon system, associated with a hadronic shower detected in the SciFi and hadronic calorimeter (Figure 34). As discussed in Section 2.2.2, muons that interact with the tungsten target generate hadronic showers as well, mimicking the ν_μ CCDIS if they do not cross the veto active area, as shown in the event displays in Figures 35 and 36. Muon DIS events are therefore topologically similar to ν_μ CC interactions, making the background events difficult to differentiate from the signal using simple selection criteria.

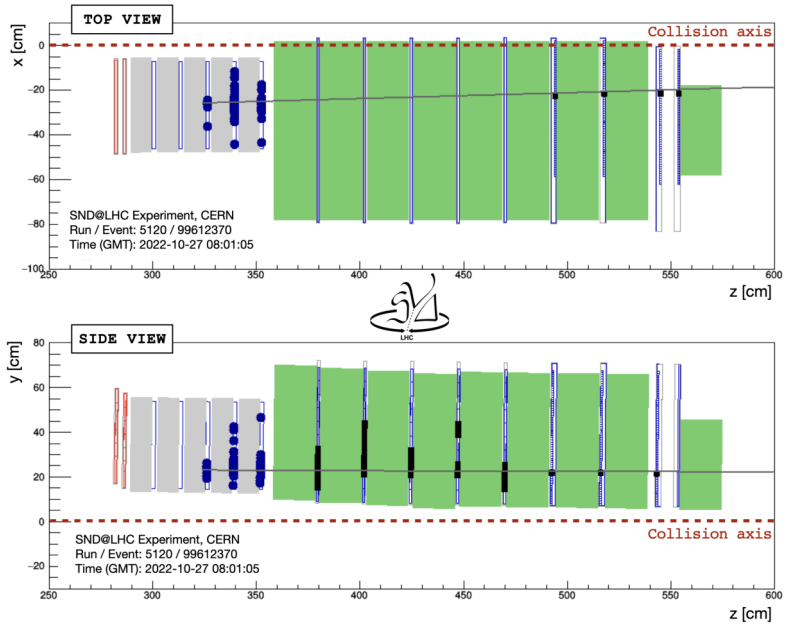

Figure 34: Display of a ν_μ CC candidate event from 2022 data. Hits in SciFi are represented as blue markers, whereas hits in the hadronic calorimeter and muon system are represented as black bars. The line represents the reconstructed muon track [52].

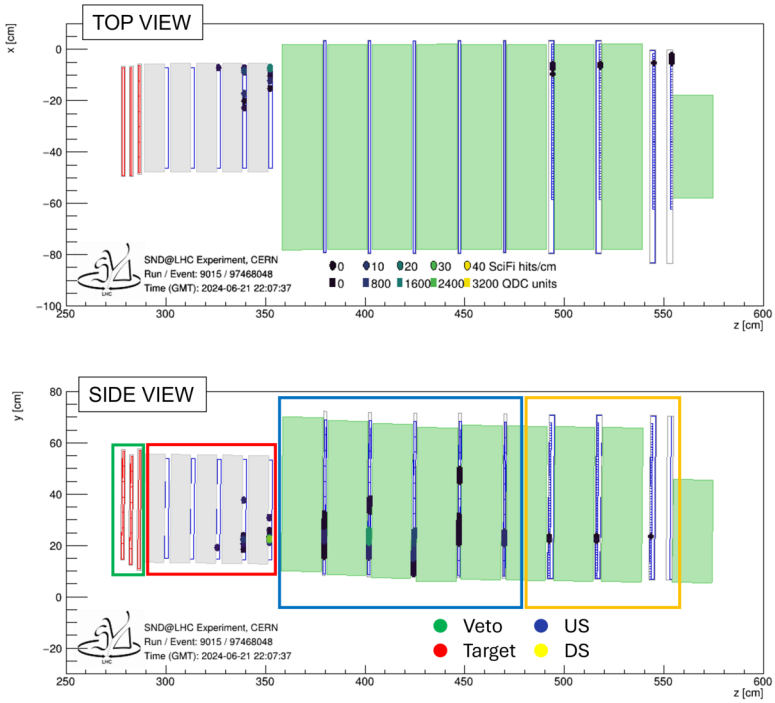

Figure 35: Display of a muon candidate from 2024 data entering the detector from the side without crossing the veto active area.

This study was performed in support of the ongoing ν_μ analysis on 2024 data [72] with the goal of evaluating the contribution of muon DIS events to the background. In this analysis, the criteria used to select a sample of CC neutrino interaction candidate events are:

- no hits in the veto system;
- event synchronised with the interaction at IP1 to reject events not originating from the main proton-proton collisions;
- selection of hits based on their time measurement to exclude noise and other instrumental effects producing hits not related to the products of the neutrino interaction;
- all US planes have some activity to ensure the muon produced in the CCDIS reaches the DS planes;
- a shower tagged in the target, using a hit-based algorithm [73];
- a reconstructed muon track that satisfies additional criteria:

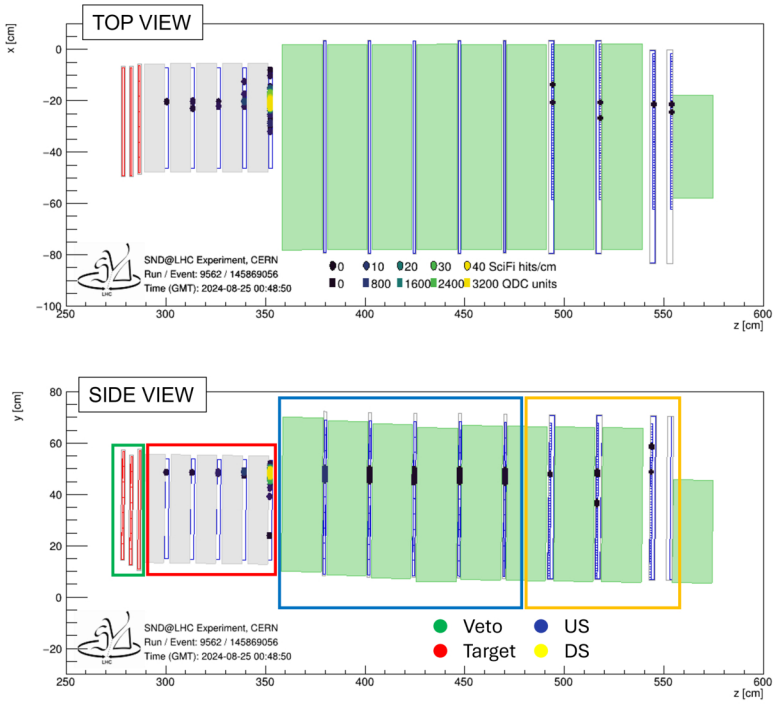

Figure 36: Display of a muon candidate from 2024 data entering the detector without leaving activity in the veto, despite the high efficiency reached with the installation of the third plane [56].

- the track is successfully reconstructed;
- reduced $\chi^2 \leq 5$;
- the track moves in the correct direction through the detector, rejecting backward-going particles from DS to SciFi.

In addition, a sample of events useful to study the features of muon background is extracted from 2024 data taking looking for a muon entering and exiting the detector and a shower in the target region, using the following criteria:

- at least two veto hits;
- at least one hit in x and y direction in at least two DS planes;
- a shower tagged in the target.

Multiple MC samples were used in this analysis to study the modelling of muon DIS events and to evaluate their agreement with the data. As a preliminary study, two samples were taken into account; their differences will be discussed in the following

Section. In both cases, the simulation implements the 2022/2023 detector geometry, corresponding to the pre–veto upgrade configuration; for this reason, they are not suitable for the validation of the ν_μ analysis on 2024 data. Nevertheless, they were used for code development purposes and to assess the impact of different simulation criteria on the characteristics of muon DIS events. The 2024 muon DIS sample was recently made available; it includes significant updates in the simulation chain and the implementation of the Monte Carlo Event Builder described in Section 3.4. In all samples, a weighting procedure is applied to each event to account for the normalization to a given luminosity and the interaction probability of the primary muon. The weight is calculated differently for each sample due to the evolution of the simulation chain and the modelling of the DIS cross section.
A comparative study was performed to assess the impact of different simulation configurations on the main features of the DIS events. The following features are examined in detail:

- position of the interaction point, to study the development of the hadronic shower;
- hit timing information, to investigate the temporal distribution of detector hits associated with muon DIS events;
- hit multiplicity, to assess the activity produced in the detector by the muon interaction.

4.2 DIS vertex position

As mentioned in Section 3.3, simulated particles are represented by `MCTrack` objects containing kinematic and spatial features, as well as information about the primary particle responsible for the interaction producing the particle under study. For each simulated event, the primary muon or antimuon that initiates the DIS is stored as the first entry in the `MCTrack` collection. At the interaction point, the DIS of the primary muon results in a hadronic shower and a secondary (scattered) muon. The secondary muon carries the same PDG code as the incoming particle but has a lower energy and a deflected trajectory. In this analysis, the DIS interaction vertex is defined as the production point of this secondary muon track. The coordinates are given in the SND@LHC reference system:

- the origin is located at 480 m from IP1;
- the z axis lies on the beam axis;
- the y axis is perpendicular to the LHC machine plane;
- the x axis is perpendicular to y and z and points to the centre of LHC.

First 2022/2023 geometry sample In this sample, muon-neutron and muon-proton interactions were simulated in a longitudinal range $z \in [-2.2; 5.8]$ m, covering the tungsten target, the Muon Filter system, and the surrounding environment. In the old simulation process, the primary muon is not transported through the material before the scattering, but it is generated, together with the secondary muon, directly at the DIS interaction vertex. Consequently, the incoming muon does not leave detector activity upstream of the interaction point, creating a significant discrepancy data and simulated events. The interaction vertices are spatially distributed as shown in Figure 37.

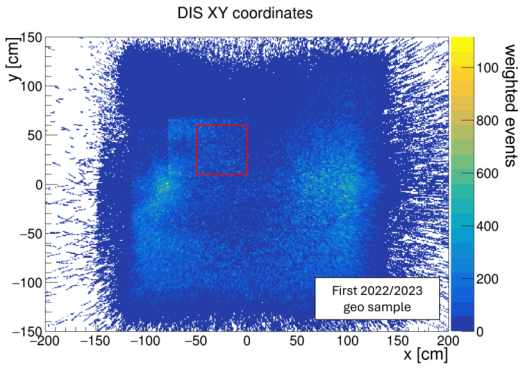

(a) XY plane.

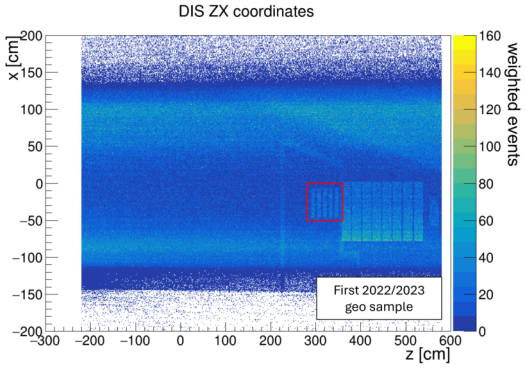

(b) ZX plane.

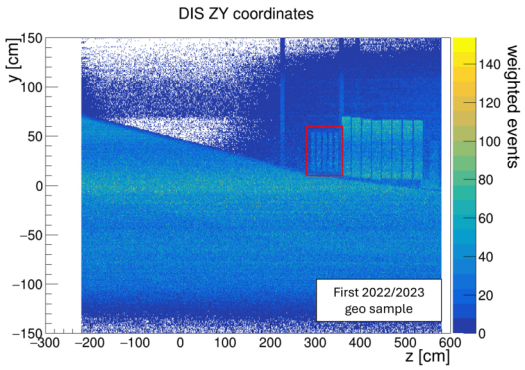

(c) ZY plane.

Figure 37: DIS coordinates for the first 2022/2023 geometry sample. The red box represents the physical boundaries of the target region.

Second 2022/2023 geometry sample This introduces a more realistic propagation model for the primary muon, which is transported from the FLUKA scoring plane (Section 3.1) through the tunnel before reaching the interaction point. This

allows for the study of activity produced by the incoming muon before the DIS. However, the simulation includes only muon-proton interactions occurring exclusively in the tungsten target. Although this sample is useful for the characterization of muon interactions in the target, the spatial constraint does not offer a realistic description in terms of background for the ν_μ analysis, since an important contribution is expected from muons interacting in the material surrounding the instrumented volume. The resulting vertex distributions are shown in Figure 38.

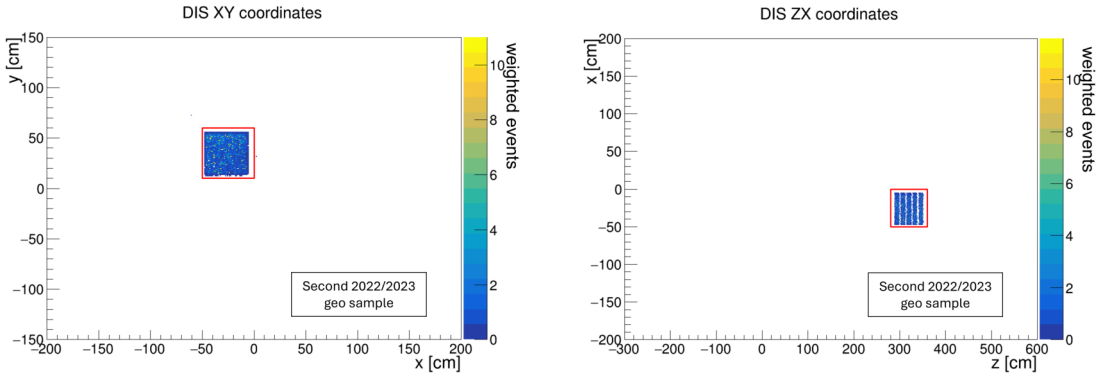

(a) XY plane.

(b) ZX plane.

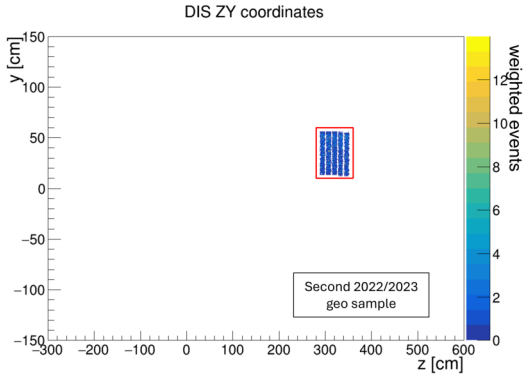

(c) ZY plane.

Figure 38: DIS coordinates for the second 2022/2023 geometry sample. The red box represents the physical boundaries of the target region.

2024 geometry sample This sample simulates muon-proton interactions in the longitudinal range $z \in [-2.2; 5.8]$ m, as shown in Figure 39, with a realistic primary muon propagation from the FLUKA scoring plane. To optimize the simulation in the rock, an energy cut of 1 GeV is used, since particles of this energy produced

away from the detector will be absorbed before reaching it. No energy threshold is used for DIS interactions in the detector. This sample provides the most complete description of the muon DIS background to date, simulating the activity before the DIS as well as background contributions from interactions outside the target. Moreover, by implementing the MCEB for the first time, this sample offers a more realistic simulation of the detector response. The MCEB also filters secondary particles that are produced and absorbed within the passive material without crossing the active area. The event topology and the development of the hadronic shower are influenced by the energy spectrum of the incoming muon, shown in Figure 40.

Since the previous samples do not offer a realistic description of the background, all results presented in the following sections refer to the latest sample.

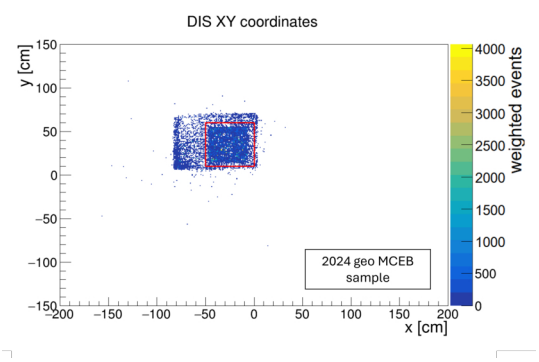

(a) XY plane.

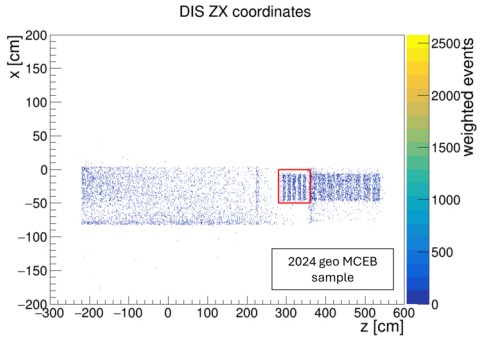

(b) ZX plane.

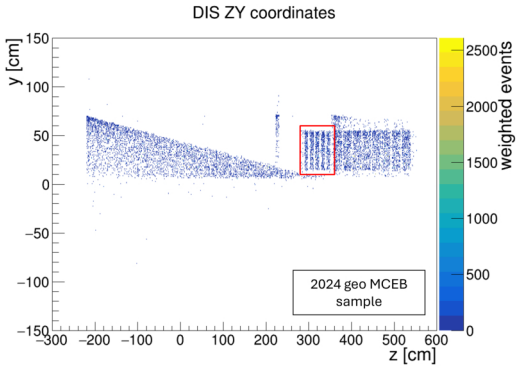

(c) ZY plane.

Figure 39: DIS coordinates for the 2024 geometry sample with MCEB. The red box represents the physical boundaries of the target region. Events are normalized to a luminosity of 1 fb^{-1}.

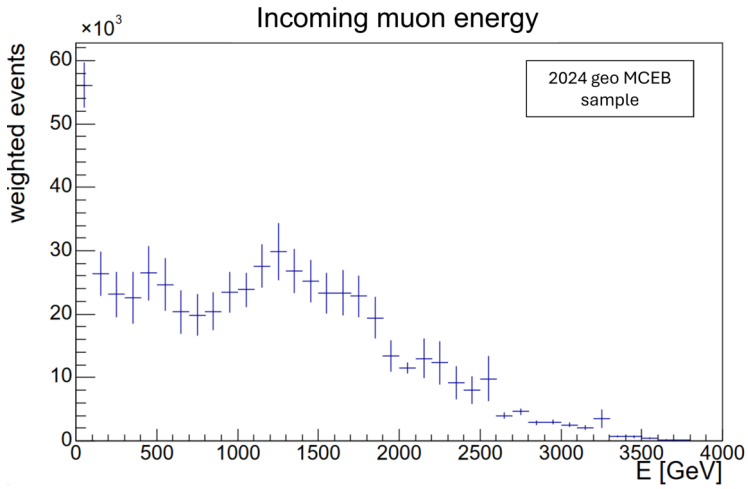

Figure 40: Energy spectrum of the incoming muon for the 2024 geometry MCEB sample. Events are normalized to a luminosity of 1 fb^{-1}.

4.2.1 Shower starting station

To characterize the longitudinal development of the hadronic shower produced in the scattering, the DIS vertex is associated to a specific SciFi station. Given the $(x,\ y,\ z)$ coordinates of the interaction, the starting station of the hadronic shower is determined by comparing the DIS position with the physical boundaries of the five stations. If the DIS coordinates fall within the volume defined by the SciFi plane i and its preceding tungsten wall, the shower is categorised as originating in station i. This mapping is essential in the study of hit multiplicity, discussed in Section 4.4. Figure 41 shows the starting station of the hadronic shower associated with the MC interaction vertex.

4.3 Hit timing

The time distribution of hits is fundamental for grouping energy depositions into physics events and to distinguish prompt signal hits from background.

In the 2022/2023 geometry samples, hit timing was simulated by applying a Gaussian smearing to the MC truth time. This approach emulates detector resolution but it is not compatible with SND@LHC DAQ system, creating unrealistic tails in the hit timestamp distribution.

With the introduction of the MCEB, the simulation evolved to a more realistic description of the hit timing, grouping MC points into 25 ns windows rather than just smearing the individual timestamps and, therefore, aligning the simulation with the DAQ logic used in the experiment. Currently, the MCEB saves only a

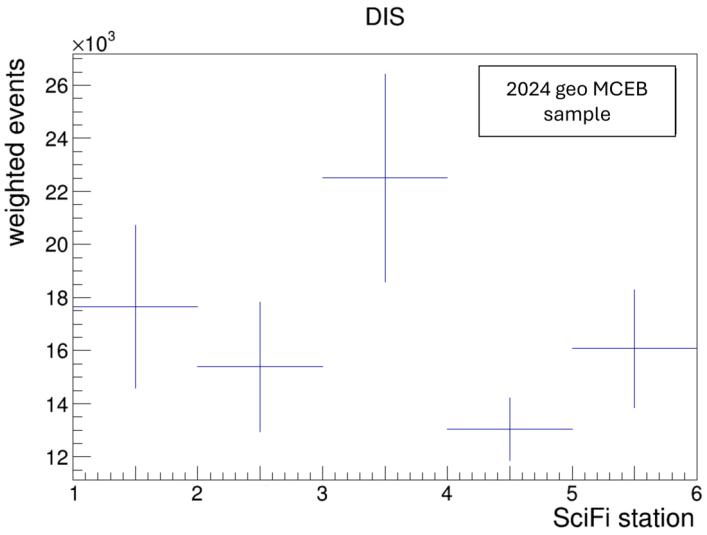

Figure 41: Shower starting station given by the DIS position. Events are normalized to a luminosity of 1 fb^{-1}.

25 ns window, as described in Section 3.4, filtering out delayed components and focusing on the prompt activity of the interaction.

Figure 42 shows the hit timing distributions in SciFi for the 2024 geometry sample before and after the implementation of the MCEB. The sharp peak represents the hits associated with the primary interaction at the DIS vertex; the spread is related to the development of the shower as it traverses the detector.

In the ν_μ analysis on 2024 data, timing selections are used to reject backgrounds and secondary delayed signals induced by afterglow or cross-talk effects. It should be noted that these hardware effects are not implemented in the simulation; hence, in the MC no further time cuts are applied. By implementing the MCEB, the simulation ensures that the hit multiplicity (discussed in Section 4.4) is not affected by out-of-time hits, i.e. activity from particles that in the simulation would continue to be tracked until their energy reaches zero. In the real detector, such delayed hits would either be lost due to SiPM deadtime, rejected by the DAQ noise filters, or excluded by preliminary analysis cuts.

4.4 Hit multiplicity

The hit multiplicity is the primary observable used in the data analysis to identify the hadronic shower produced in a DIS interaction. Understanding the relationship between the interaction vertex and the resulting hit distribution is fundamental for the evaluation and rejection of the muon DIS background. Figure 43 shows

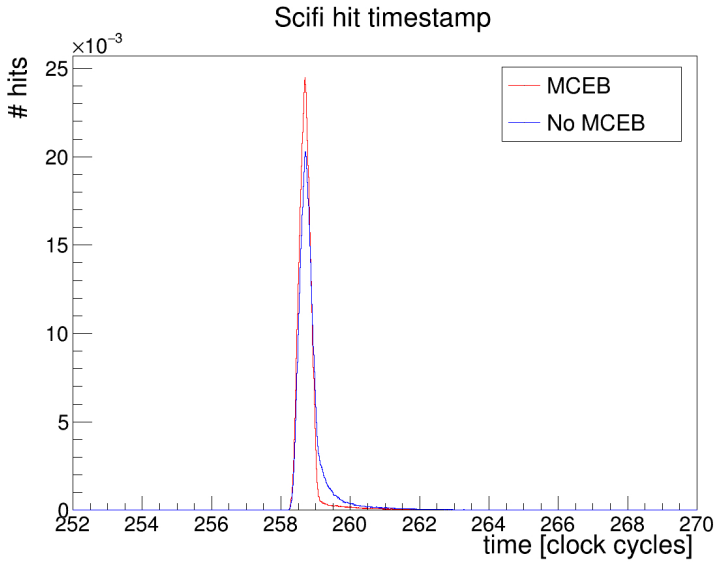

Figure 42: Hit timing for SciFi 2024 geometry sample before (blue) and after (red) the implementation of the MCEB measured in clock cycles (1 clock cycle = 6.25 ns). The distributions are normalized to unity for shape comparison.

the average number of the sum of x and y hits per SciFi plane, categorised by the true MC DIS vertex position. These profiles reflect the behaviour of the hadronic shower, with a sharp increase of the number of hits in correspondence of the DIS interaction vertex and a subsequent decay. The presence of non negligible activity in the stations prior the DIS hints at the contribution from additional processes which will be addressed in this Section.

4.4.1 Shower tagging algorithm

The shower tagging algorithm was developed to identify showers and to estimate their origin using a hit density method [73]. The algorithm is configured to search for at least 10 hits within a 128-channel sliding window (corresponding to ~ 3.2 cm) out of the 1536 of each plane, in both the x and y directions of each SciFi plane in the target.

To optimize the algorithm, the stations in which a shower is tagged were compared with the true MC DIS vertex stations discussed in Section 4.2.1. Given that a DIS interaction has occurred in a specific SciFi station, the efficiency ϵ represents the probability that the algorithm successfully tags a shower in that station. As shown in the efficiency plot in Figure 44, the algorithm maintains a stable efficiency at about 70% across all stations.

The fraction of events that are not tagged might be due to different reasons,

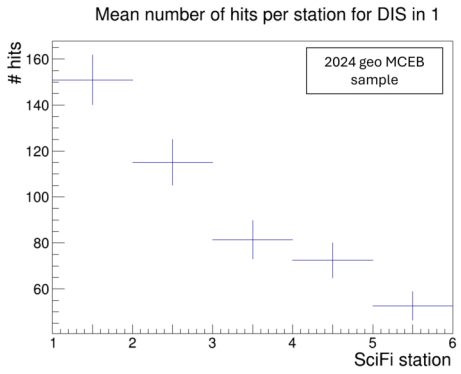

(a) Hits per station for DIS in SciFi 1.

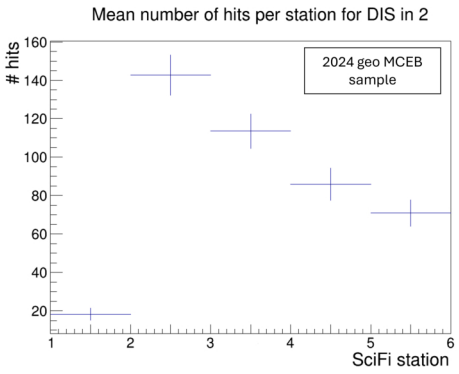

(b) Hits per station for DIS in SciFi 2.

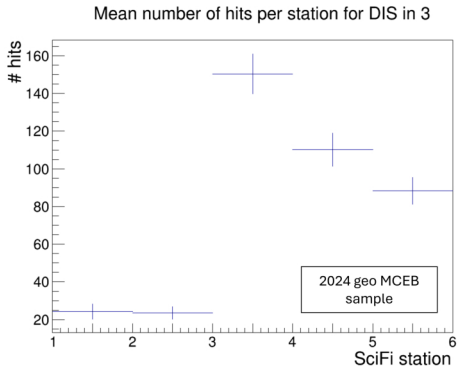

(c) Hits per station for DIS in SciFi 3.

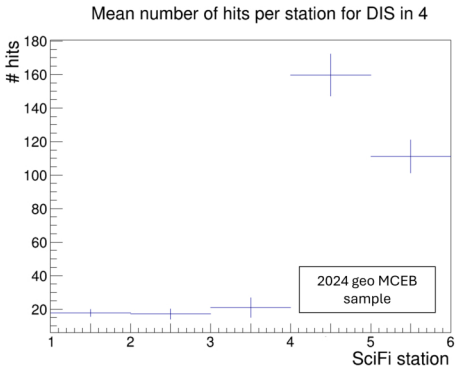

(d) Hits per station for DIS in SciFi 4.

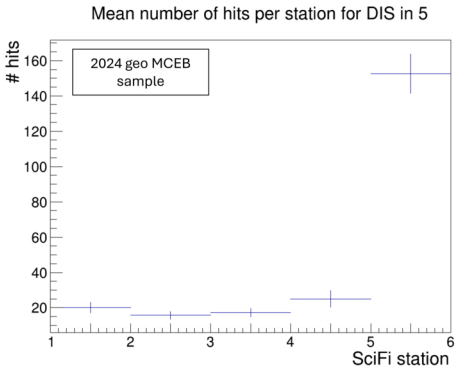

(e) Hits per station for DIS in SciFi 5.

Figure 43: Mean number of hits per SciFi plane, categorised by the MC DIS vertex position.

such as lateral shower leakage for DIS interactions occurring near the edge of the station or insufficient development of the shower for DIS interactions near the downstream end of the station.

The efficiency is also related to the energy of the incoming muon, as shown in Figure 45. The efficiency increases with the energy, as lower-energy DIS interactions produce hadronic showers with lower particle multiplicity, which might not satisfy the algorithm's requirements.

The tagged shower start, whose distribution is shown in Figure 46, is defined as the most upstream SciFi plane in which a shower is tagged via the hit density. The correlation between the reconstructed starting station and the MC DIS vertex station is shown in Figure 47. Although a diagonal correlation is visible, a fraction of events the algorithm tags the shower start before or after the physical DIS interaction.

Regarding showers tagged as starting after the DIS station, these are classified as such mainly because they had not yet developed sufficiently to meet the requirement of the shower tagging algorithm.

On the other hand, when the shower start is tagged upstream of the DIS station, the algorithm is tagging secondary activity produced by the incoming muon before it

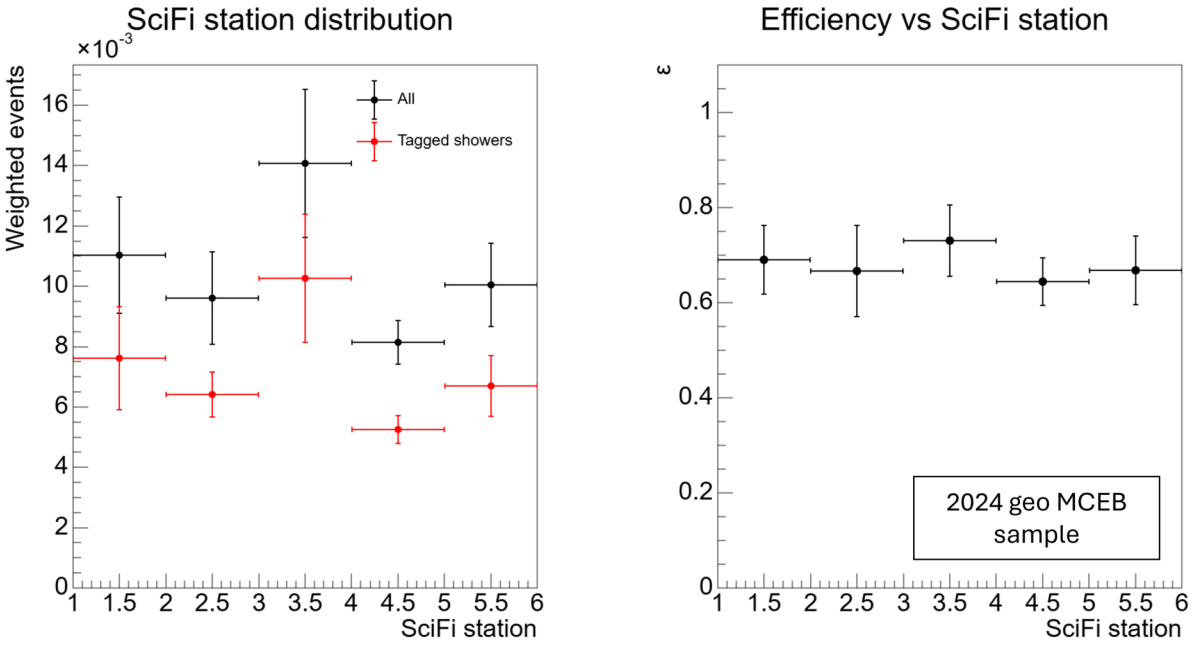

Figure 44: Left: DIS stations for all muons (black) and for those with a shower tagged in the DIS stations (red). Right: Shower tag algorithm efficiency ϵ for each SciFi station.

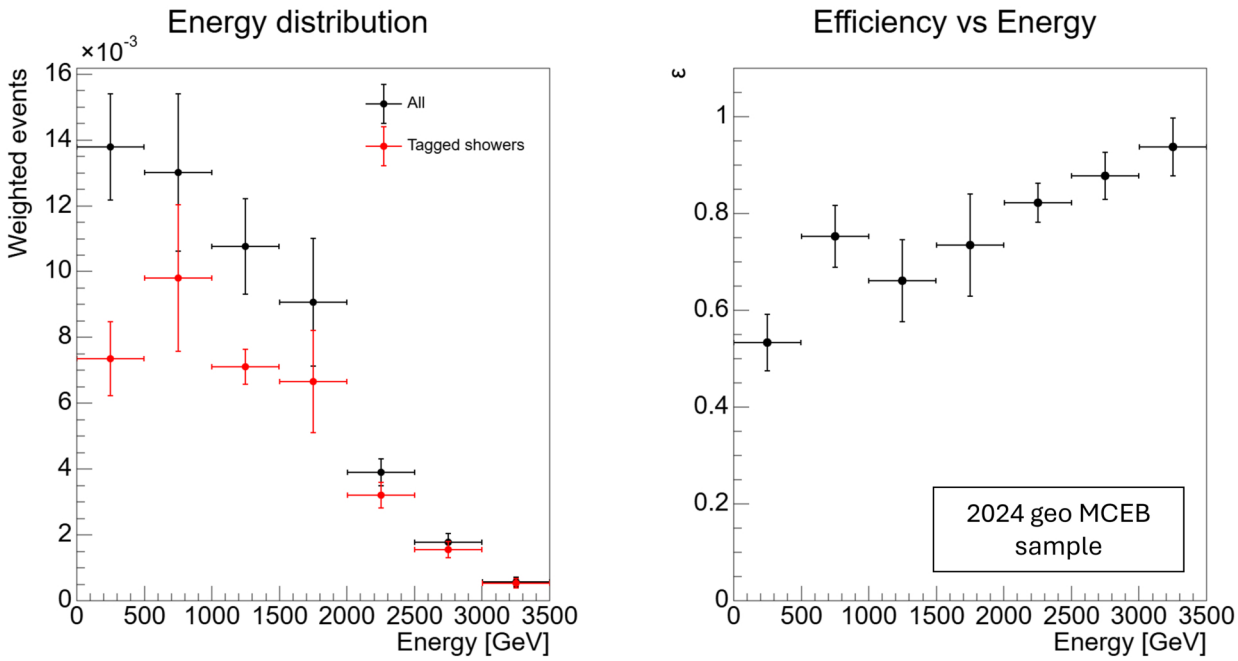

Figure 45: Left: energy distribution of all incoming muons interacting in the target (black) and of those with a shower tagged in the DIS station (red). Right: shower tag algorithm efficiency ϵ as a function of the incoming muon energy.

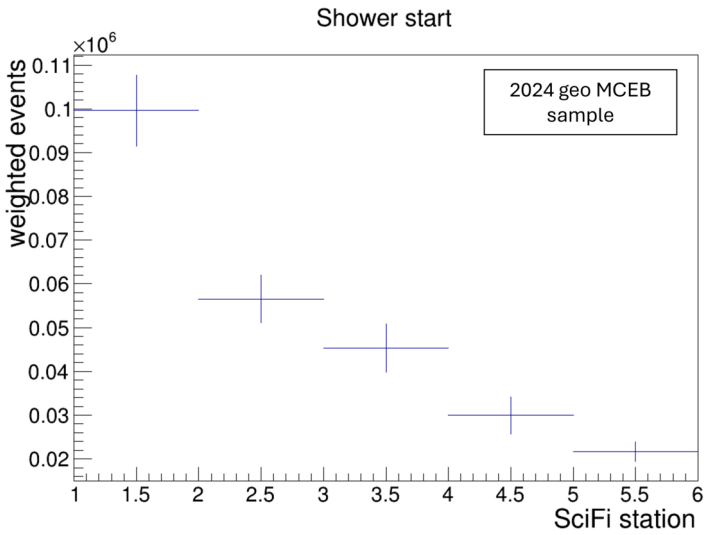

Figure 46: Shower starting station given by the shower tagging algorithm. Events are normalized to a luminosity of 1 fb^{-1}.

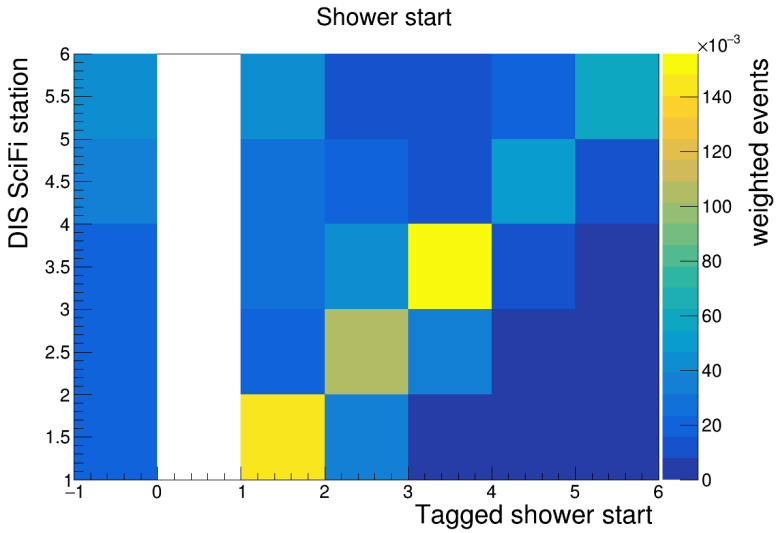

Figure 47: Correlation between the reconstructed starting station (x axis) and MC DIS vertex station (y axis). The value -1 for the tagged shower start refers to showers not tagged in the target. The distribution is normalized to unity.

undergoes the DIS interaction. These events, although correctly tagged as showers, represent a background for the study of the DIS hadronic shower; they might arise from various processes, such as:

- lepton pair production, which initiates electromagnetic showers;
- δ electrons knocked out of the atomic shells of the tungsten target, which can create hit clusters that satisfy the algorithm requirement;
- Compton scattering, which results in additional charged particles contributing to the hit multiplicity;
- bremsstrahlung, which initiates electromagnetic showers.

As an example, the secondary processes that occur before the scattering in SciFi 4 are shown in Figure 48. Lepton pair production is the dominant contributor to the early signals, and it is highly localised in the station immediately preceding the true interaction vertex. Thus, to study the hadronic showers produced in DIS events, it is necessary to reject the electromagnetic showers initiated by the primary muon when crossing the detector.

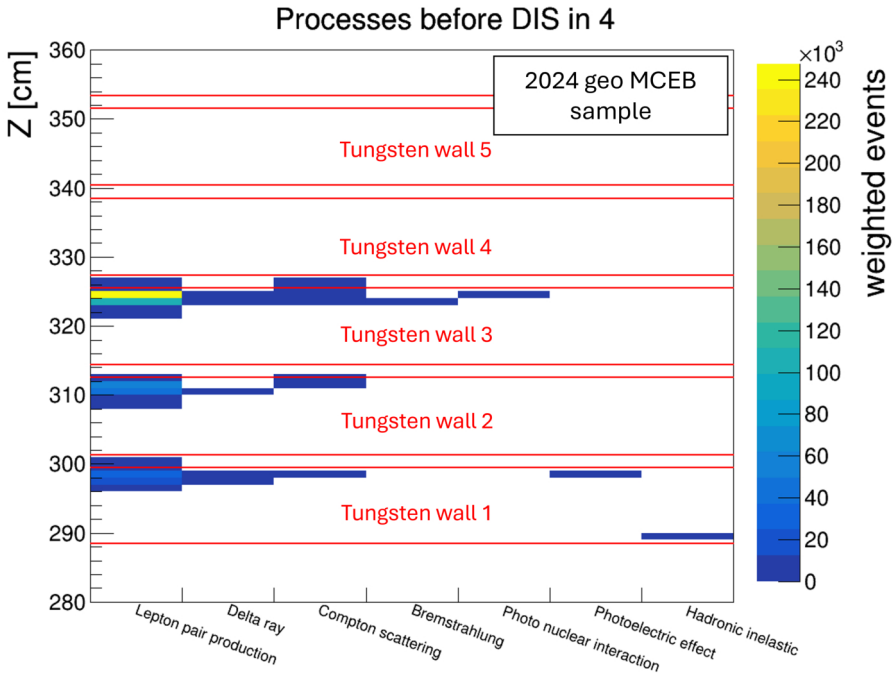

Figure 48: Secondary processes before DIS in SciFi 4.

4.4.2 Strict shower tagging

To reduce the contribution from electromagnetic showers, stricter constraints were added to the shower tagging algorithm.

The additional requirements are based on the different longitudinal development of hadronic and electromagnetic showers. Typically, hadronic showers extend over $6 - 9\ \lambda_{int}$ to reach 95% containment. Since a single tungsten wall in the target covers $\sim 0.5\ \lambda_{int}$, the shower is expected to develop across multiple stations. On the other hand, electromagnetic showers reach 95% containment within $15 - 20\ X_0$. As a single tungsten wall covers $\sim 17\ X_0$, most electromagnetic showers are contained within a single SciFi station, and their contribution can be reduced requiring that two consecutive stations meet the shower tagging criteria.

For SciFi 5, this requirement cannot be applied, as it is the last SciFi wall; therefore, shower development must be observed in the US planes and the algorithm needs to be adapted to account for shower development in iron, rather than of tungsten (Section 2.3.4). The requirement chosen to validate a SciFi 5 shower tag is to have at least 6 bars with signal in the entire US system [72].

As in the original shower tagging case, to evaluate the efficiency of the "strict" shower tag the stations in which a shower is tagged are compared with the true MC DIS vertex stations. As before, given that a DIS interaction has occurred in a

specific SciFi station, the efficiency ϵ, shown in Figure 49, represents the probability that the strict algorithm successfully tags a shower in the station. As expected, due to the additional requirements, the overall efficiency is decreased; however, in SciFi 5 the efficiency value is slightly different, suggesting a possible effect due to the involvement of the US system. The efficiency as a function of the incoming muon energy is presented in Figure 50; as expected, also in this case the efficiency increases with the energy.

The strict shower start, whose distribution is shown in Figure 51, is defined as the most upstream SciFi plane that meets the additional requirements. The correlation between this reconstructed starting station and the MC vertex station is shown in Figure 52. Despite the more stringent selection, a fraction of events with a shower start tagged before the MC shower start is still present. This contribution is mainly due to cases where multiple electromagnetic showers occur in consecutive stations, satisfying the strict shower start algorithm requirements.

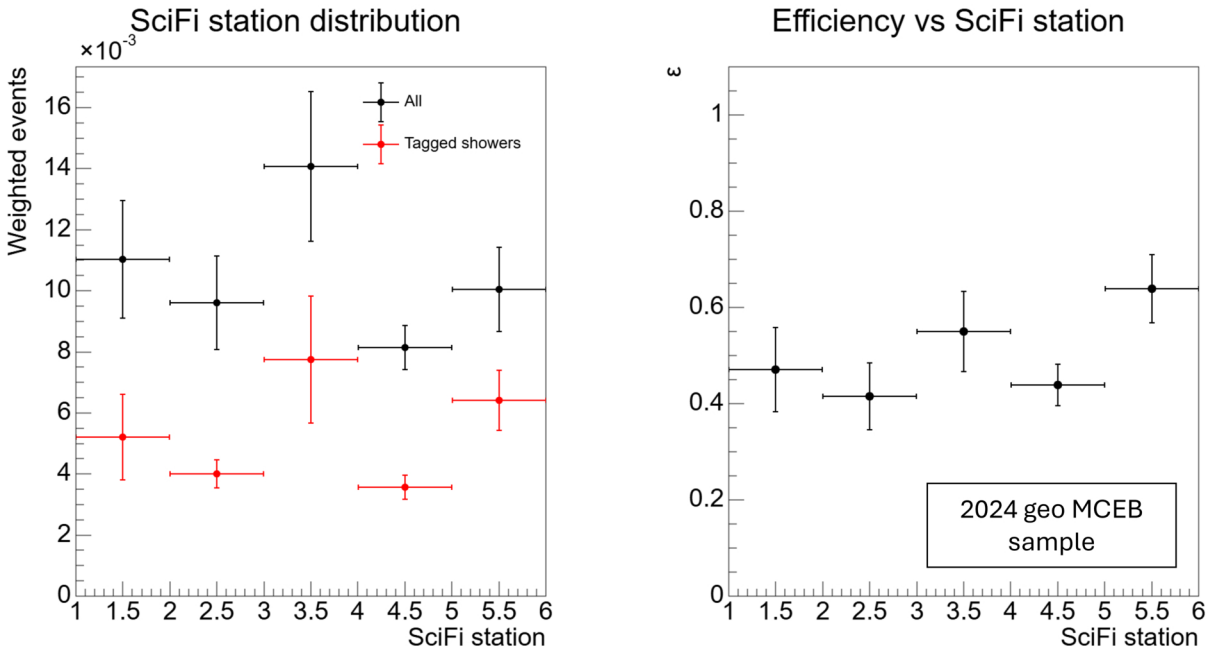

Figure 49: Left: DIS stations for all muons (black) and for those with a shower tagged in the DIS stations with the strict algorithm (red). Right: Strict shower tag algorithm efficiency ϵ for each SciFi station.

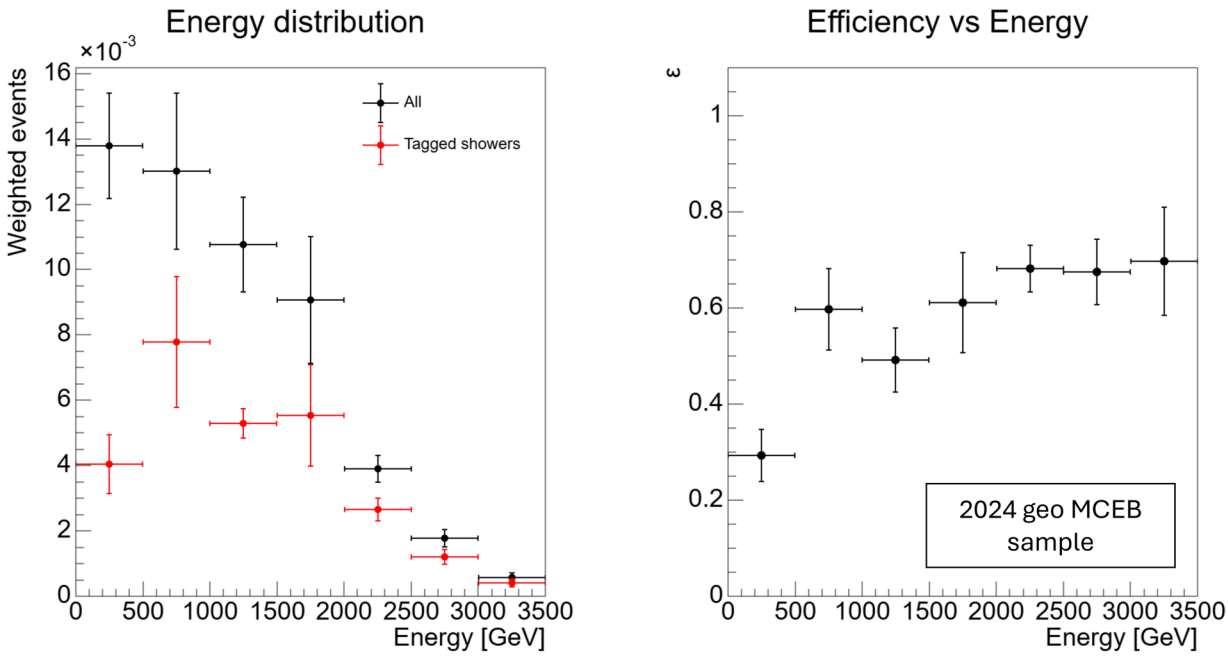

Figure 50: Left: energy distribution of all incoming muons interacting in the target (black) and of those with a shower tagged in the DIS station with the strict algorithm (red). Right: strict shower tag algorithm efficiency ϵ as a function of the incoming muon energy.

4.4.3 Comparison with 2024 data

The final stage of this characterization involves a direct comparison between the 2024 MCEB simulation and the 2024 data starting from the number of hits, which is the main observable used to identify showers. The muon data sample consists of the events preselected using the criteria defined in Section 4.1.

The initial comparison revealed a discrepancy in the hit multiplicity in SciFi, which was significantly higher in the MC than in the data, as shown in Figure 53. This might arise from an over sensitivity of the simulation which leads to the digitization of low-energy depositions that the physical detector electronics would actually suppress. To better understand the origin of this disagreement between MC and data, the energy depositions contributing to the digitized hits were studied (the `Digi_ScifiHit2MCPoints` described in Section 3.3).

Since electromagnetic showers often produce additional activity in the detector before the DIS, an overestimation of low-energy electrons may lead to the observed excess of SciFi hits in the MC. As discussed in Section 3.3, the digitization process uses a nominal threshold of 3.5 photoelectrons (p.e.), corresponding to an energy

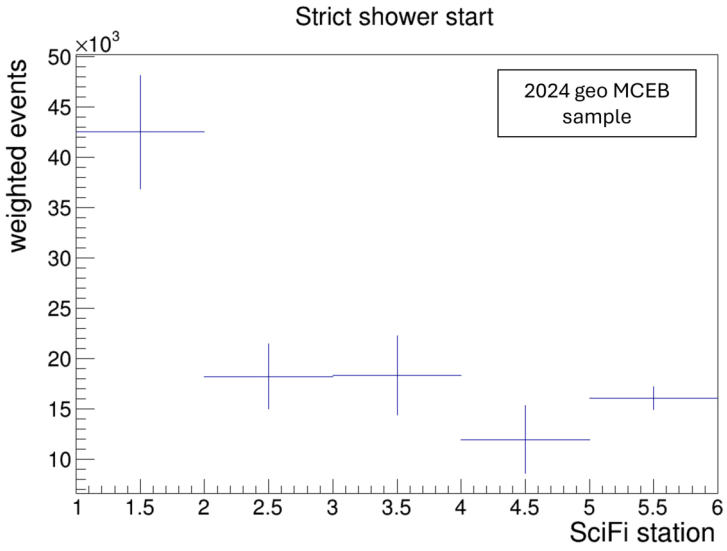

Figure 51: Shower starting station given by the "strict" shower tagging. Events are normalized to a luminosity of 1 fb^{-1}.

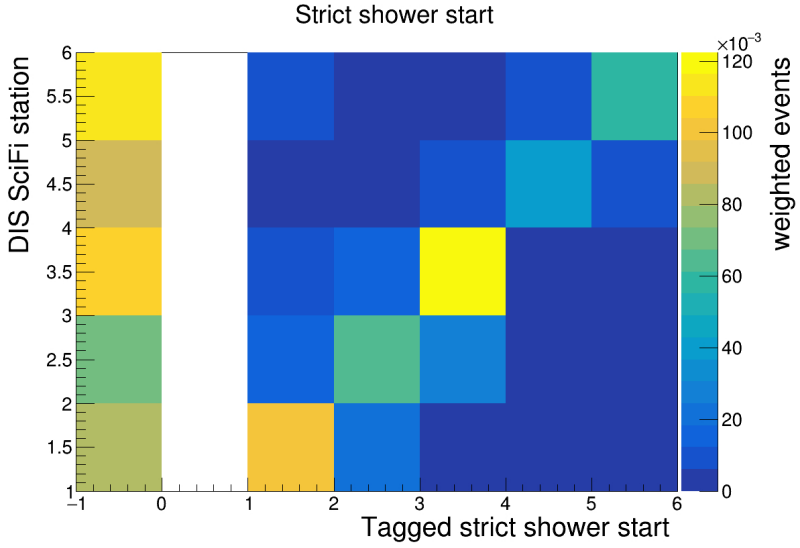

Figure 52: Correlation between the reconstructed "strict" shower starting station (x axis) and MC DIS vertex station (y axis). The value -1 for the tagged shower start refers to showers not tagged in the target. The distribution is normalized to unity.

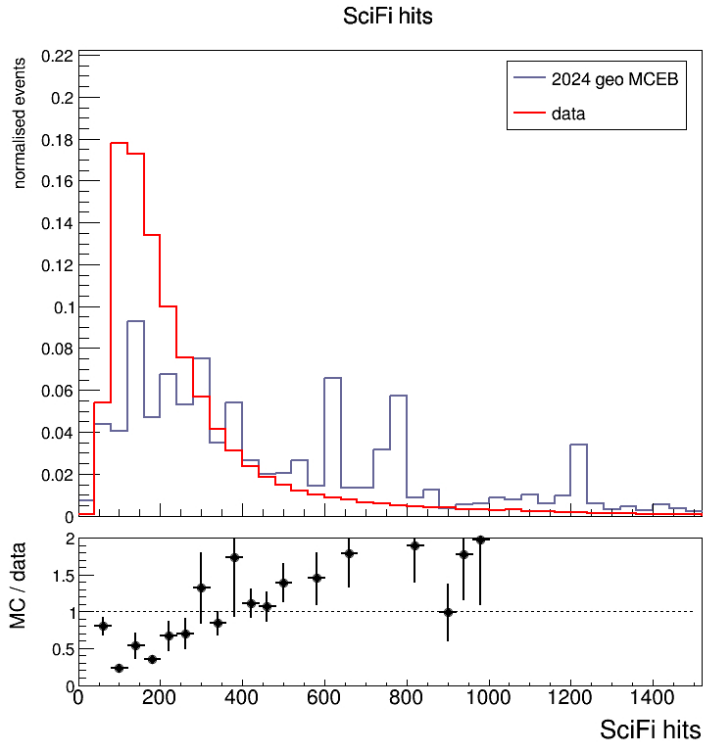

Figure 53: Distribution of SciFi hits for experimental data from Run 8323 (red) and the 2024 geometry MCEB sample (grey). The bottom panel shows the MC/data ratio, highlighting the discrepancy between the two.

of about 22 keV deposited per particle. To address the disagreement between data and MC in the number of hits, a threshold scan was performed to find a higher cut that suppresses the low-energy electron contributions without losing the signal from the primary muon. Figure 54 shows the relevant part of the spectrum of the MC points contributing to each SciFi hit for incoming muons and electrons. Thresholds from 1 to 30 p.e. were tested; the vertical lines in the plot indicate 3 (used as a proxy of the default value), 5, and 7 photoelectrons.

The threshold scan was performed starting from a sample of passing muons. These events provide the benchmark for tuning digitization parameters as they consist of well-defined tracks with minimal secondary activity compared to DIS events. A muon crossing a SciFi station typically produces a cluster of 2 hits in both x and y planes, resulting in 4 hits per station. To maximize the statistics for the threshold scan, the passing muon sample was extracted from the MC sample by analysing the primary muon track before any interaction. As for the experimental data, the passing muon sample was selected by requiring activity in all veto and US planes and the absence of a tagged shower in the target. Figure 55 shows the

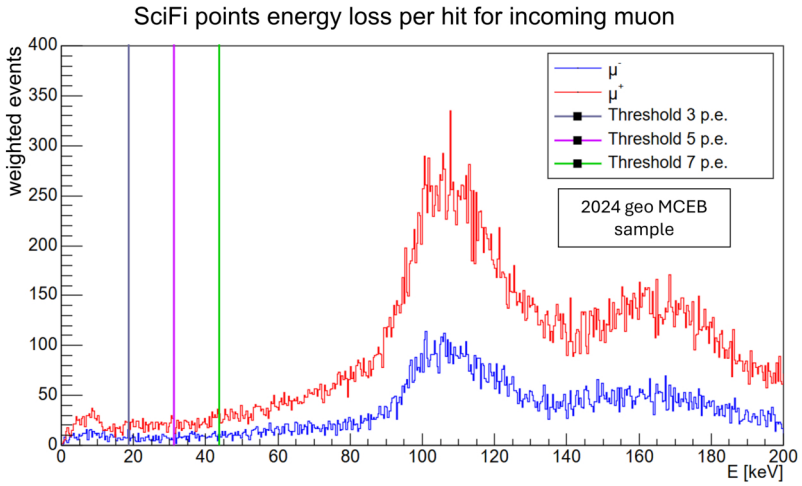

(a) Incoming muons.

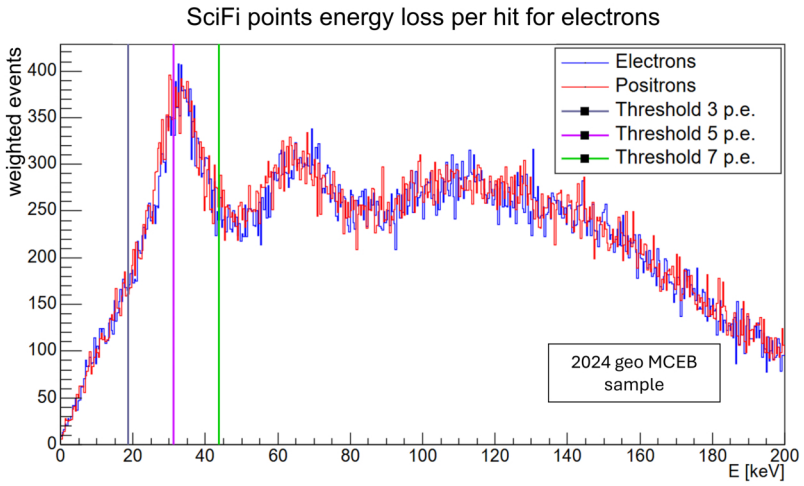

(b) Electrons and positrons.

Figure 54: Energy depositions per SciFi hit for incoming muons (a) and electrons produced in interactions (b) in keV. The vertical lines represent the 3 (grey), 5 (violet) and 7 (green) p.e. thresholds, converted in keV.

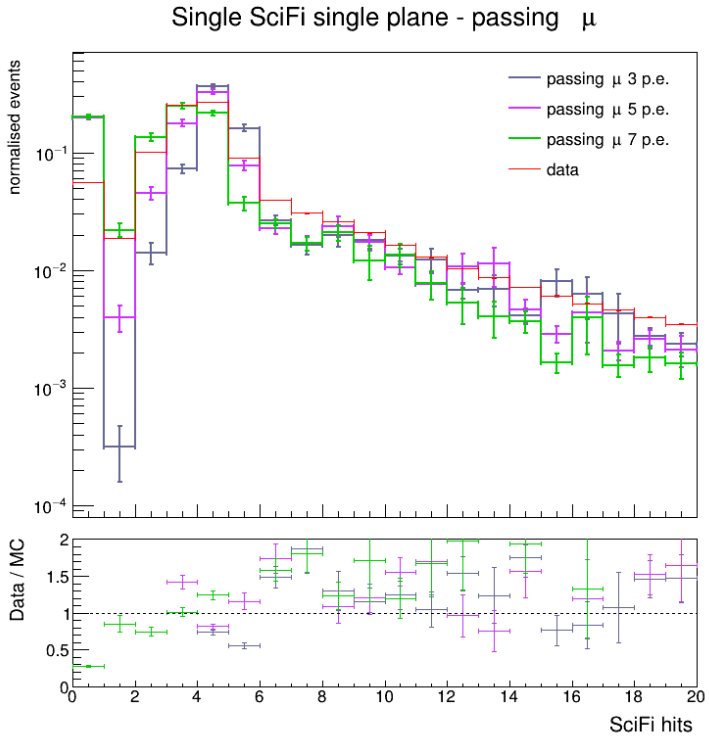

Figure 55: Distributions of SciFi hits multiplicity per plane for passing muons. The experimental data (red) are compared with MC samples simulated using different digitization threshold: 3 (grey), 5 (violet), and 7 (green) photoelectrons.

SciFi hit distribution for passing muons in data compared to MC samples with the different thresholds. The nominal threshold leads to an excess of the number of hits around the peak, indicating that additional low-energy depositions are being digitized in the simulation. Increasing the threshold, the effect is slightly reduced; from an analysis of the reduced χ^2 computed with the bin-per-bin difference between data and the available threshold samples, whose distribution is shown in Figure 56, 5 p.e. was found to be the best. The range used for this study was restricted from 1 to 15 hits in the SciFi plane due to lack of events for the higher threshold values.

To confirm that the over-sensitivity to low-energy secondary electron depositions is the main cause behind the hit multiplicity discrepancy in DIS events, electromagnetic (EM) showers need to be studied. For the MC sample, events were selected where the DIS interaction occurs downstream of the SciFi stations, ensuring that the activity in the target is purely electromagnetic. For the experimental data, the sample was selected by requiring hits in all veto and US planes, a shower tagged as starting in SciFi 2 or 3 and contained within a single station, and the number of hits in SciFi 1 between 2 and 6, to reject noise or lateral events, as the ones shown

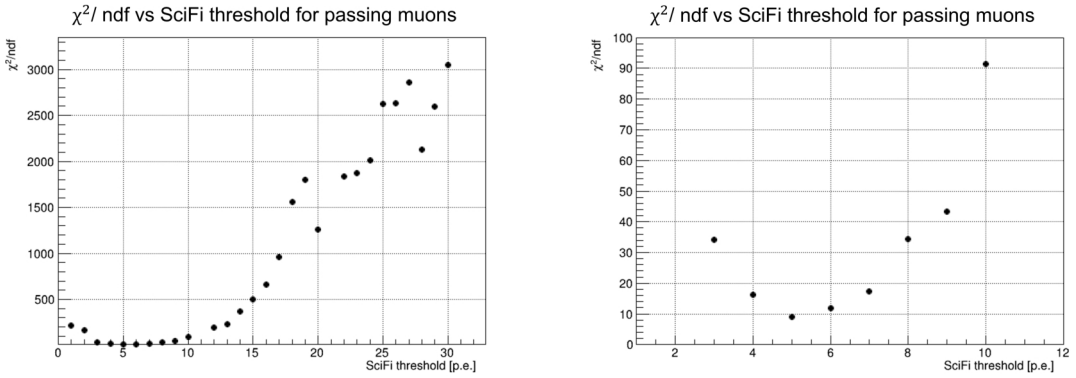

Figure 56: Distribution of the reduced χ^2 for passing muons as a function of different thresholds. The plot on the right shows a zoomed in version, showing the minimum at 5 photoelectrons.

in Figure 57. The distribution of SciFi hit multiplicity for electromagnetic showers is shown in Figure 58 for the different digitization thresholds. The discrepancy is particularly pronounced at intermediate and high multiplicities, especially for the 3 p.e. threshold. Comparing the histograms with the same method previously described, the best threshold for the digitization found with the EM showers sample is 7 photoelectrons. However, at high multiplicity a clear discrepancy between data and simulation remains for all thresholds.

As for hadronic showers, they differ significantly from electromagnetic ones, as shown in Figure 59, hence the sensitivity to the digitization thresholds may be different. To isolate hadronic shower activity, in the MC sample only events where the DIS interaction occurs in the target were selected. Furthermore, events, both in data and MC, are required to have a shower tagged in three consecutive SciFi planes, ensuring that the observed signal corresponds to a hadronic shower. The number of hits in the middle plane is taken as a reference for the MC-data comparison. As observed in Figure 60, the various thresholds do not impact the distribution as in the electromagnetic case, indicating that the hit multiplicity is mostly insensitive to the digitization threshold.

Since the threshold tuning fails to resolve the discrepancy in hit multiplicity between MC and data in hadronic showers produced in the DIS interaction, the results suggest that the origin of the disagreement lies upstream of the detector response modelling and point at a difference in the simulation of the physical process within the detector.

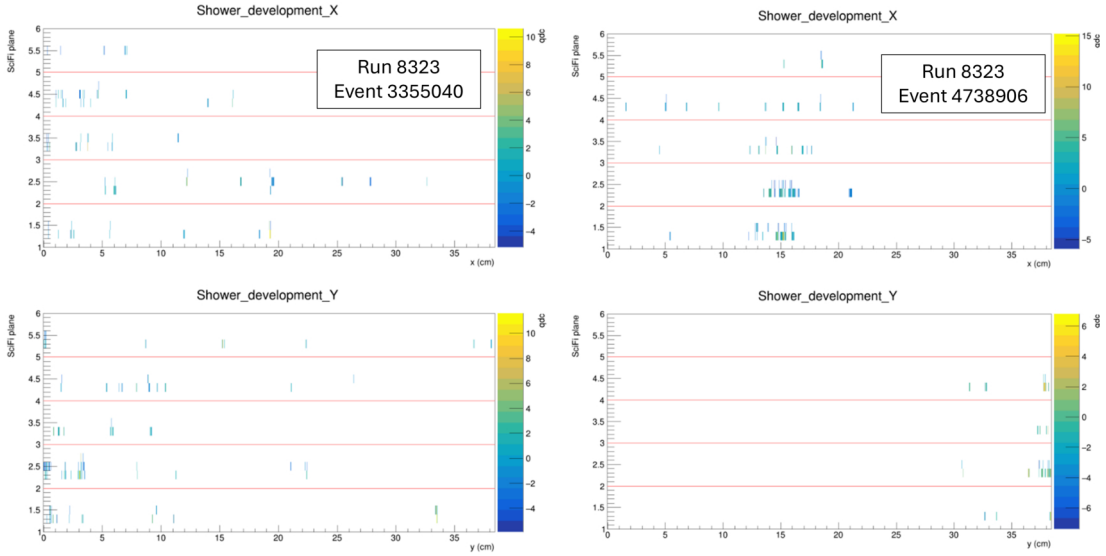

(a) Noise event.

(b) Lateral event.

Figure 57: Display of noise (a) and lateral (b) muon events from Run 8323 excluded in the selection of electromagnetic showers. The red lines indicate the SciFi planes, ordered from bottom to top; each band is further subdivided into five bins, each corresponding to one clock cycle, while the colour scale encodes the digitized charge information. The top panels show the shower development in the x direction, whereas the bottom panels show the shower development in the y direction.

4.5 Outlook

The studies presented in this chapter represent a first step toward the characterization of the muon DIS simulation with the 2024 geometry. Although a new threshold for the digitization slightly improves the agreement between the number of hits in MC and data for the electromagnetic component, additional improvements are needed to solve the residual hadronic discrepancies.
Further analyses should focus on improving the discrimination between electromagnetic and hadronic showers. The development of the shower has been shown to be insufficient for this goal; consequently, other variables need to be investigated, such as:

- shower compactness, analysing the lateral spread of the shower;
- further studies on hit density, evaluating the concentration of the fired channels to distinguish the more compact electromagnetic showers from the sparse topology of the hadronic ones;

- energy deposited in each channel, identifying high-energy depositions from hadronic fragments.

Ongoing studies within the Collaboration proposed different approaches to improve the agreement between data and MC, such as the implementation of cuts on MC energy deposits and a refinement of the simulation chain. In particular, the future improvements include an update of the GEANT4 parameters, switching from an energy cut to a range cut for the treatment of low-energy particles, and a change of the list of processes enabled in the GEANT4 configuration, to achieve a more accurate modelling of the energy depositions from both electromagnetic and hadronic showers.

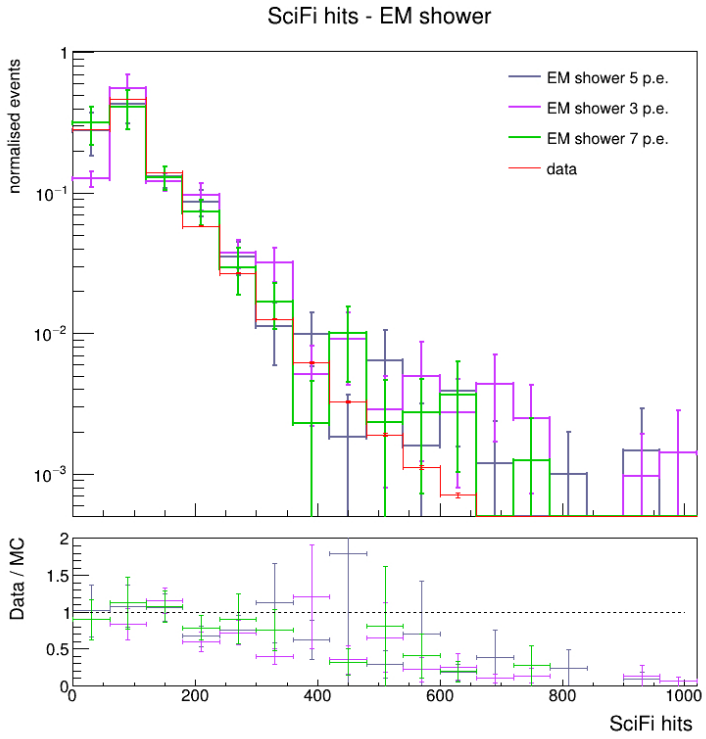

Figure 58: Distributions of SciFi hits multiplicity for electromagnetic showers. The experimental data (red) are compared with MC samples simulated using different digitization thresholds: 3 (grey), 5 (violet), and 7 (green) photoelectrons.

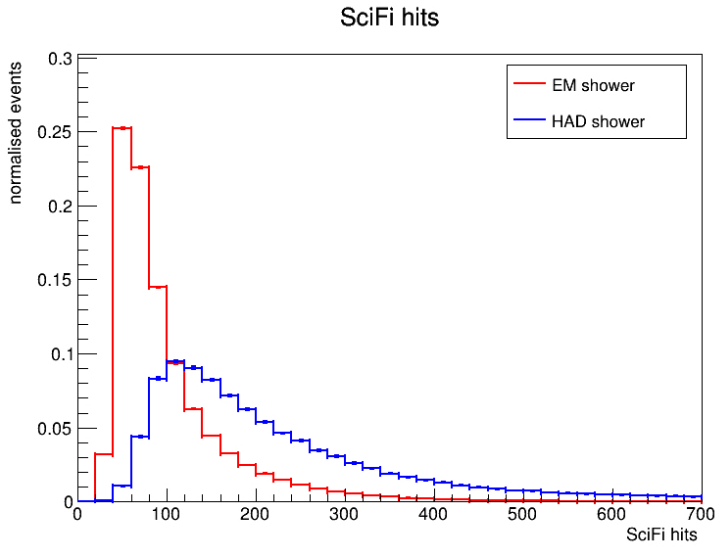

Figure 59: Number of SciFi hits for electromagnetic and hadronic showers in data.

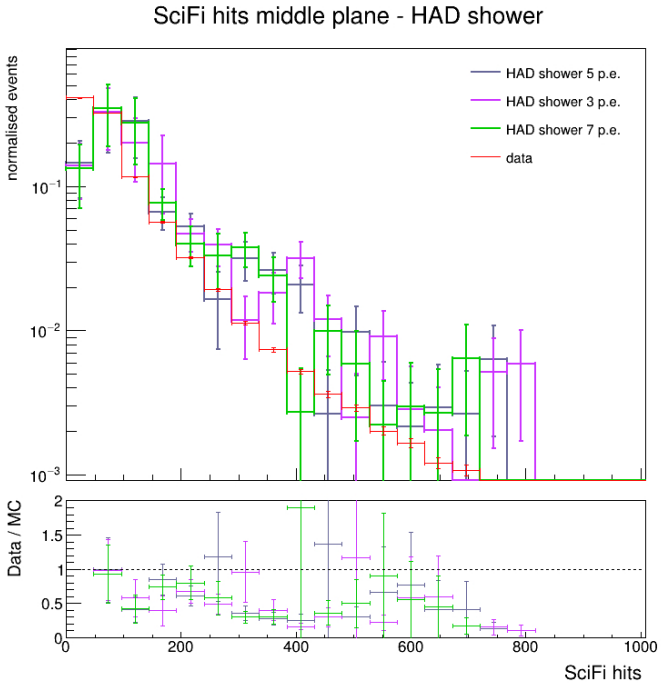

Figure 60: Distribution of SciFi hits multiplicity for hadronic showers, in the second of the three consecutive planes in which a shower is tagged. The experimental data (red) are compared with MC samples simulated using different digitization thresholds: 3 (grey), 5 (violet), and 7 (green) photoelectrons.

Conclusions

The SND@LHC experiment aims to identify high-energy neutrinos of all three flavours, produced in proton-proton collisions, in the pseudorapidity range $7.2 < \eta < 8.4$. In the context of the ν_μ analysis, the main background is induced by high-energy muons undergoing deep inelastic scattering (DIS) within the tungsten target, as these events can mimic ν_μ charged-current interactions.

This thesis provided a preliminary characterization of muon DIS events using Monte Carlo (MC) simulations. Several samples were used to assess the impact of the various upgrades of the simulation chain; however, for a comparison between 2024 data and MC, in this work only the most recent sample is treated in detail. In addition to a more realistic propagation of the primary muons and simulation of the DIS events, the latest sample includes the implementation of the Monte Carlo Event Builder, in which the grouping of MC energy depositions into 25 ns windows aligns the simulation with the data acquisition logic used in the experiment.

The study of the DIS topology allows for a validation of the shower tagging algorithm, developed to identify showers in the target region exploiting a hit density method. The performance of the algorithm is evaluated using the true position of the interaction vertex, from which the shower originates, from the MC simulation. The efficiency is found to be stable across all stations, and positively correlated with the energy of the interacting muon, as expected since low-energy muons produce hadronic showers with smaller multiplicity.

The study also revealed that several electromagnetic processes can occur upstream of the DIS interaction. To reject electromagnetic showers, more stringent requirements were applied to the algorithm. The "strict" shower start successfully excludes some of the misclassified electromagnetic showers; nevertheless, several events in which showers are tagged before the DIS interaction are present, mainly due to the contribution from electromagnetic showers occurring in consecutive stations.

A preliminary comparison with data collected in 2024 revealed a discrepancy in the hit multiplicity in SciFi, which resulted in a higher value in the MC than in the data. In order to verify the hypothesis that such discrepancy originated in the modelling of the digitization process, a scan of the digitization threshold was performed, evaluating quantitatively the data-MC agreement for each tested threshold value. After performing the scan on passing muons and electromagnetic shower events, in which a higher threshold mitigated the difference in the number of hits, the same procedure on hadronic shower events showed that in this case the hit multiplicity is mostly insensitive to the digitization threshold.

Ongoing studies within the Collaboration proposed different approaches to improve the agreement between data and MC and a new sample is currently being

developed. The new simulation chain includes an update of the GEANT4 energy thresholds and the list of physics processes for a more accurate modelling of low-energy particles and all involved physical processes. The work presented in this thesis can be used to assess the improvements introduced with the update of the simulation and to continue the work on the validation of the ν_μ analysis on 2024 data.

Bibliography

[1] W. Pauli. "Dear radioactive ladies and gentlemen". In: *Phys. Today* 31N9 (1978), p. 27.

[2] J. Chadwick. "The existence of a neutron". In: *Proceedings of the Royal Society of London. Series A, Containing Papers of a Mathematical and Physical Character* 136.830 (June 1932), pp. 692–708. ISSN: 0950-1207. DOI: 10.1098/rspa.1932.0112.

[3] E. Fermi. "Tentativo di una teoria dei raggi beta". In: *Il Nuovo Cimento* 11 (1934), pp. 1–19. DOI: https://doi.org/10.1007/BF02959820.

[4] C. L. Cowan et al. "Detection of the Free Neutrino: a Confirmation". In: *Science* 124.3212 (1956), pp. 103–104. DOI: 10.1126/science.124.3212.103.

[5] S. H. Neddermeyer and C. D. Anderson. "Note on the Nature of Cosmic-Ray Particles". In: *Phys. Rev.* 51 (10 May 1937), pp. 884–886. DOI: 10.1103/PhysRev.51.884.

[6] G. Feinberg. "Decays of the μ Meson in the Intermediate-Meson Theory". In: *Phys. Rev.* 110 (6 June 1958), pp. 1482–1483. DOI: 10.1103/PhysRev.110.1482.

[7] S. Frankel et al. "New Limit on the $e + \gamma$ Decay Mode of the Muon". In: *Phys. Rev. Lett.* 8 (3 Feb. 1962), pp. 123–125. DOI: 10.1103/PhysRevLett.8.123.

[8] G. Danby et al. "Observation of High-Energy Neutrino Reactions and the Existence of Two Kinds of Neutrinos". In: *Phys. Rev. Lett.* 9 (1 July 1962), pp. 36–44. DOI: 10.1103/PhysRevLett.9.36.

[9] B. Pontecorvo. "Electron and Muon Neutrinos". In: *Zh. Eksp. Teor. Fiz.* 37 (1959), pp. 1751–1757.

[10] M. L. Perl et al. "Evidence for Anomalous Lepton Production in $e^+ - e^-$ Annihilation". In: *Phys. Rev. Lett.* 35 (22 Dec. 1975), pp. 1489–1492. DOI: 10.1103/PhysRevLett.35.1489.

[11] DONUT Collaboration. "Observation of tau neutrino interactions". In: *Physics Letters B* 504.3 (Apr. 2001), pp. 218–224. ISSN: 0370-2693. DOI: 10.1016/s0370-2693(01)00307-0.

[12] C. Wu et al. "Experimental Test of Parity Conservation in Beta Decay". In: *Phys. Rev.* 105 (4 Feb. 1957), pp. 1413–1415. DOI: 10.1103/PhysRev.105.1413.

[13] L. Landau. "On the conservation laws for weak interactions". In: *Nuclear Physics* 3.1 (1957), pp. 127–131. DOI: https://doi.org/10.1016/0029-5582(57)90061-5.

[14] A. Salam. "On parity conservation and neutrino mass". In: *Nuovo Cim.* 5 (1957), pp. 299–301. DOI: 10.1007/BF02812841.

[15] T. D. Lee and C. N. Yang. "Parity Nonconservation and a Two-Component Theory of the Neutrino". In: *Phys. Rev.* 105 (5 Mar. 1957), pp. 1671–1675. DOI: 10.1103/PhysRev.105.1671.

[16] M. Goldhaber et al. "Helicity of Neutrinos". In: *Phys. Rev.* 109 (3 Feb. 1958), pp. 1015–1017. DOI: 10.1103/PhysRev.109.1015.

[17] A. Roy. "Helicity of the neutrino: Determination of the nature of weak interaction". In: *Resonance* 20 (Aug. 2015), pp. 699–710. DOI: 10.1007/s12045-015-0227-y.

[18] S. L. Glashow. "Partial-symmetries of weak interactions". In: *Nuclear Physics* 22 (4 1961), pp. 579–588. DOI: https://doi.org/10.1016/0029-5582(61)90469-2.

[19] S. Weinberg. "A Model of Leptons". In: *Phys. Rev. Lett.* 19 (21 Nov. 1967), pp. 1264–1266. DOI: 10.1103/PhysRevLett.19.1264.

[20] A. Salam. "Weak and Electromagnetic Interactions". In: *Conf. Proc. C* 680519 (1968), pp. 367–377. DOI: 10.1142/9789812795915_0034.

[21] M. Thomson. *Modern Particle Physics*. Cambridge University Press, 2013.

[22] Particle Data Group Collaboration. "Review of Particle Physics". In: *Phys. Rev. D* 110 (3 Aug. 2024). DOI: 10.1103/PhysRevD.110.030001.

[23] F. Englert and R. Brout. "Broken Symmetry and the Mass of Gauge Vector Mesons". In: *Phys. Rev. Lett.* 13 (9 Aug. 1964), pp. 321–323. DOI: 10.1103/PhysRevLett.13.321.

[24] P. W. Higgs. "Broken symmetries, massless particles and gauge fields". In: *Phys. Lett.* 12 (1964), pp. 132–133. DOI: 10.1016/0031-9163(64)91136-9.

[25] P. W. Higgs. "Broken Symmetries and the Masses of Gauge Bosons". In: *Phys. Rev. Lett.* 13 (16 Oct. 1964), pp. 508–509. DOI: 10.1103/PhysRevLett.13.508.

[26] J. A. Formaggio and G. P. Zeller. "From eV to EeV: Neutrino cross sections across energy scales". In: *Reviews of Modern Physics* 84.3 (Sept. 2012), pp. 1307–1341. ISSN: 1539-0756. DOI: 10.1103/revmodphys.84.1307.

[27] A. Ariga et al. "Neutrino Experiments at the Large Hadron Collider". In: *Annual Review of Nuclear and Particle Science* 75.1 (Sept. 2025), pp. 57–81. ISSN: 1545-4134. DOI: 10.1146/annurev-nucl-121423-101000.

[28] LHCf Collaboration. "Measurement of forward photon production cross-section in proton–proton collisions at $\sqrt{s} = 13\,\text{TeV}$ with the LHCf detector". In: *Physics Letters B* 780 (2018), pp. 233–239. ISSN: 0370-2693. DOI: https://doi.org/10.1016/j.physletb.2017.12.050. URL: https://www.sciencedirect.com/science/article/pii/S0370269317310365.

[29] LHCf Collaboration. "Measurement of inclusive forward neutron production cross section in proton-proton collisions at $\sqrt{s} = 13$ TeV with the LHCf Arm2 detector". In: *Journal of High Energy Physics* 2018.11 (Nov. 2018). ISSN: 1029-8479. DOI: 10.1007/jhep11(2018)073. URL: http://dx.doi.org/10.1007/JHEP11(2018)073.

[30] C. Giunti and M. Laveder. *Neutrino mixing*. Oct. 2003. arXiv: hep-ph/0310238.

[31] S. Bilenky. *Neutrinos: Majorana or Dirac?* 2020. arXiv: 2008.02110 [hep-ph].

[32] E. Majorana. "Teoria simmetrica dell'elettrone e del positrone". In: *Nuovo Cim.* 14 (1937), pp. 171–184. DOI: 10.1007/BF02961314.

[33] B. Pontecorvo. "Mesonium and Antimesonium". In: *Sov. Phys. JETP* 6 (1958), pp. 429–431.

[34] Z. Maki, M. Nakagawa, and S. Sakata. "Remarks on the Unified Model of Elementary Particles". In: *Progress of Theoretical Physics* 28.5 (Nov. 1962), pp. 870–880. DOI: 10.1143/PTP.28.870.

[35] Homestake Collaboration. "Measurement of the solar electron neutrino flux with the Homestake chlorine detector". In: *Astrophys. J.* 496 (1998), pp. 505–526. DOI: 10.1086/305343.

[36] GNO Collaboration. "Complete results for five years of GNO solar neutrino observations". In: *Physics Letters B* 616.3-4 (June 2005), pp. 174–190. ISSN: 0370-2693. DOI: 10.1016/j.physletb.2005.04.068.

[37] SNO Collaboration. "Direct Evidence for Neutrino Flavor Transformation from Neutral-Current Interactions in the Sudbury Neutrino Observatory". In: *Phys. Rev. Lett.* 89.1 (June 2002). ISSN: 1079-7114. DOI: 10.1103/physrevlett.89.011301.

[38] Super-Kamiokande Collaboration. "Evidence for Oscillation of Atmospheric Neutrinos". In: *Phys. Rev. Lett.* 81.8 (Aug. 1998), pp. 1562–1567. ISSN: 1079-7114. DOI: 10.1103/physrevlett.81.1562.

[39] KamLAND Collaboration. "Measurement of Neutrino Oscillation with KamLAND: Evidence of Spectral Distortion". In: *Phys. Rev. Lett.* 94.8 (Mar. 2005). ISSN: 1079-7114. DOI: 10.1103/physrevlett.94.081801.

[40] Double Chooz Collaboration. "First measurement of θ_{13} from delayed neutron capture on hydrogen in the Double Chooz experiment". In: *Physics Letters B* 723.1-3 (June 2013), pp. 66–70. ISSN: 0370-2693. DOI: 10.1016/j.physletb.2013.04.050.

[41] C. Ahdida et al. *SND@LHC - Scattering and Neutrino Detector at the LHC*. Tech. rep. Geneva: CERN, 2021. URL: https://cds.cern.ch/record/2750060.

[42] SND@LHC Collaboration. "SND@LHC: the Scattering and Neutrino Detector at the LHC". In: *Journal of Instrumentation* 19.05 (2024). ISSN: 1748-0221. DOI: 10.1088/1748-0221/19/05/p05067. URL: http://dx.doi.org/10.1088/1748-0221/19/05/P05067.

[43] M. Bustamante and A. Connolly. "Extracting the Energy-Dependent Neutrino-Nucleon Cross Section above 10 TeV Using IceCube Showers". In: *Phys. Rev. Lett.* 122 (4 Jan. 2019), p. 041101. DOI: 10.1103/PhysRevLett.122.041101. URL: https://link.aps.org/doi/10.1103/PhysRevLett.122.041101.

[44] LHCb collaboration. "Measurements of prompt charm production cross-sections in pp collisions at $\sqrt{13}$ TeV". In: *Journal of High Energy Physics* 159 (Mar. 2016). DOI: 10.1007/JHEP03(2016)159.

[45] S. Alekhin et al. "A facility to search for hidden particles at the CERN SPS: the SHiP physics case". In: *Reports on Progress in Physics* 79.12 (Oct. 2016), p. 124201. DOI: 10.1088/0034-4885/79/12/124201. URL: https://doi.org/10.1088/0034-4885/79/12/124201.

[46] G. De Lellis, P. Migliozzi, and P. Santorelli. "Charm physics with neutrinos". In: *Physics Reports* 399.5 (2004), pp. 227–320. ISSN: 0370-1573. DOI: https://doi.org/10.1016/j.physrep.2004.07.005.

[47] A. Di Crescenzo and G. Galati. "SND@LHC: A New Experiment in Neutrino Physics at the LHC". In: *Symmetry* 15.6 (2023). ISSN: 2073-8994. DOI: 10.3390/sym15061256. URL: https://www.mdpi.com/2073-8994/15/6/1256.

[48] N. Beni et al. "Physics potential of an experiment using LHC neutrinos". In: *Journal of Physics G: Nuclear and Particle Physics* 46.11 (2019), p. 115008. DOI: 10.1088/1361-6471/ab3f7c. URL: https://dx.doi.org/10.1088/1361-6471/ab3f7c.

[49] N. Beni et al. "Further studies on the physics potential of an experiment using LHC neutrinos". In: *Journal of Physics G: Nuclear and Particle Physics* 47.12 (Nov. 2020). DOI: 10.1088/1361-6471/aba7ad. URL: https://dx.doi.org/10.1088/1361-6471/aba7ad.

[50] T. Sjöstrand et al. “An introduction to PYTHIA 8.2”. In: *Computer Physics Communications* 191 (2015). ISSN: 0010-4655. DOI: 10.1016/j.cpc.2015.01.024. URL: http://dx.doi.org/10.1016/j.cpc.2015.01.024.

[51] FASER Collaboration. *FASER: ForwArd Search ExpeRiment at the LHC*. 2019. arXiv: 1901.04468 [hep-ex]. URL: https://arxiv.org/abs/1901.04468.

[52] SND@LHC Collaboration. “Observation of Collider Muon Neutrinos with the SND@LHC Experiment”. In: *Phys. Rev. Lett.* 131 (3 July 2023), p. 031802. DOI: 10.1103/PhysRevLett.131.031802.

[53] S. I. Ilieva. *Measurement of the muon flux at SND@LHC*. 2023. URL: https://cds.cern.ch/record/2859193.

[54] R. Voss. “Deep-inelastic scattering with muons”. In: *Physics Reports* 403-404 (2004), pp. 3–18. ISSN: 0370-1573. DOI: https://doi.org/10.1016/j.physrep.2004.08.006.

[55] L. Mozzina. “Upgrade of the SND@LHC muon detectors with drift tubes”. MA thesis. URL: https://amslaurea.unibo.it/id/eprint/36655/.

[56] SND@LHC Collaboration. “Installation and performance of the 3rd Veto plane at the SND@LHC detector”. In: *Journal of Instrumentation* 20.07 (July 2025). ISSN: 1748-0221. DOI: 10.1088/1748-0221/20/07/p07011. URL: http://dx.doi.org/10.1088/1748-0221/20/07/P07011.

[57] G. Paggi. “Vetoing charged particles for neutrino detection at the LHC”. In: *Nuclear Instruments and Methods in Physics Research Section A: Accelerators, Spectrometers, Detectors and Associated Equipment* 1069 (2024), p. 169928. ISSN: 0168-9002. DOI: https://doi.org/10.1016/j.nima.2024.169928. URL: https://www.sciencedirect.com/science/article/pii/S0168900224008544.

[58] R. Bugalho et al. “Experimental characterization of the TOFPET2 ASIC”. In: *Journal of Instrumentation* 14.03 (Mar. 2019), P03029. DOI: 10.1088/1748-0221/14/03/P03029. URL: https://doi.org/10.1088/1748-0221/14/03/P03029.

[59] G. Battistoni et al. “Overview of the FLUKA code”. In: *Annals of Nuclear Energy* 82 (2015). Joint International Conference on Supercomputing in Nuclear Applications and Monte Carlo 2013, SNA + MC 2013. Pluri- and Trans-disciplinarity, Towards New Modeling and Numerical Simulation Paradigms, pp. 10–18. ISSN: 0306-4549. DOI: https://doi.org/10.1016/j.anucene.2014.11.007.

[60] T.T. Böhlen et al. "The FLUKA Code: Developments and Challenges for High Energy and Medical Applications". In: *Nuclear Data Sheets* 120 (2014), pp. 211–214. ISSN: 0090-3752. DOI: https://doi.org/10.1016/j.nds.2014.07.049.

[61] A. Fedynitch. *Cascade equations and hadronic interactions at very high energies*. Nov. 2015.

[62] A. Fedynitch and R. Engel. *Revision of the high energy hadronic interaction models PHOJET/DPMJET-III*. 2015. URL: https://cds.cern.ch/record/2115393.

[63] C. Andreopoulos et al. "The GENIE neutrino Monte Carlo generator". In: *Nuclear Instruments and Methods in Physics Research Section A: Accelerators, Spectrometers, Detectors and Associated Equipment* 614.1 (2010), pp. 87–104. ISSN: 0168-9002. DOI: https://doi.org/10.1016/j.nima.2009.12.009. URL: https://www.sciencedirect.com/science/article/pii/S0168900209023043.

[64] T. Sjöstrand, S. Mrenna, and P. Skands. "PYTHIA 6.4 physics and manual". In: *Journal of High Energy Physics* 2006.05 (May 2006), pp. 026–026. ISSN: 1029-8479. DOI: 10.1088/1126-6708/2006/05/026. URL: http://dx.doi.org/10.1088/1126-6708/2006/05/026.

[65] T. Sjöstrand, S. Mrenna, and P. Skands. "A brief introduction to PYTHIA 8.1". In: *Computer Physics Communications* 178.11 (2008), pp. 852–867. ISSN: 0010-4655. DOI: https://doi.org/10.1016/j.cpc.2008.01.036. URL: https://www.sciencedirect.com/science/article/pii/S0010465508000441.

[66] S. Agostinelli et al. "GEANT4-a simulation toolkit". In: *Nuclear Instruments and Methods in Physics Research Section A Accelerators Spectrometers Detectors and Associated Equipment* 506 (July 2003), p. 250. DOI: 10.1016/S0168-9002(03)01368-8.

[67] R. Brun and F. Rademakers. "ROOT — An object oriented data analysis framework". In: *Nuclear Instruments and Methods in Physics Research Section A: Accelerators, Spectrometers, Detectors and Associated Equipment* 389.1 (1997). New Computing Techniques in Physics Research V, pp. 81–86. ISSN: 0168-9002. DOI: https://doi.org/10.1016/S0168-9002(97)00048-X. URL: https://www.sciencedirect.com/science/article/pii/S016890029700048X.

[68] *sndsw*. URL: https://github.com/SND-LHC/sndsw.

[69] *FairShip*. URL: https://github.com/ShipSoft/FairShip.

[70] M. Al-Turany et al. “The FairRoot framework”. In: *Journal of Physics: Conference Series* 396.2 (Dec. 2012), p. 022001. DOI: 10.1088/1742-6596/396/2/022001. URL: https://doi.org/10.1088/1742-6596/396/2/022001.

[71] P. J. Baculima Calle. *SND@LHC: Monte Carlo Event Builder*. 2025. URL: https://cds.cern.ch/record/2949536.

[72] G. Paggi. “Upgrades of the SND@LHC detector during LHC Run 3 and search for muon neutrinos from proton–proton collisions at $\sqrt{s} = 13.6\,\text{TeV}$”. PhD thesis. Alma Mater Studiorum – Università di Bologna, 2026.

[73] SND@LHC Collaboration. “Studies of hadronic showers in SND@LHC”. In: *Journal of Instrumentation* 20.10 (Oct. 2025), P10039. DOI: 10.1088/1748-0221/20/10/P10039. URL: https://doi.org/10.1088/1748-0221/20/10/P10039.